Universidade de São Paulo
Instituto de Física

Procura por *fast radio bursts* — uma previsão para o sistema de interferometria do BINGO

Gabriel Amâncio Hoerning

Orientador: Prof. Dr. Elcio Abdalla

Dissertação de mestrado apresentada ao Instituto de Física da Universidade de São Paulo, como requisito parcial para a obtenção do título de Mestre(a) em Ciências.

Banca Examinadora:
Prof. Dr. Elcio Abdalla (IF-USP)
Prof. Dr. Alberto Vazquez Saa (UNICAMP)
Prof. Dr. Julio Cesar Fabris (UFES)

São Paulo
2023

FICHA CATALOGRÁFICA
Preparada pelo Serviço de Biblioteca e Informação do Instituto de Física da Universidade de São Paulo

Hoerning, Gabriel Amâncio

Procura por fast radio bursts — uma previsão para o sistema de interferometria do BINGO. São Paulo, 2023.

Dissertação (Mestrado) - Universidade de São Paulo. Instituto de Física. Depto. Física Geral

Orientador: Prof. Dr. Élcio Abdalla

Área de Concentração: Cosmologia.

Unitermos: 1. Radioastronomia; 2. Interferometria; 3. Cosmologia.

USP/IF/SBI-040/2023

University of São Paulo
Physics Institute

Search for fast radio bursts — a forecast for the BINGO interferometry system

Gabriel Amâncio Hoerning

Supervisor: Prof. Dr. Elcio Abdalla

Dissertation submitted to the Physics Institute of the University of São Paulo in partial fulfilment of the requirements for the degree of Master of Science.

Examining Committee:
Prof. Dr. Elcio Abdalla (IF-USP)
Prof. Dr. Alberto Vazquez Saa (UNICAMP)
Prof. Dr. Julio Cesar Fabris (UFES)

São Paulo
2023

To Bruna, who triggered a
fast pulsar heart in my chest.

Acknowledgments

I am grateful to my family for their support. They were the umbrella on a rainy day. My mother Cláudia, my stepfather Sergio, my brother Guilherme, my grandmother Arnilda, my girlfriend Bruna, and my dog Mila always supported me in the choices for my life with faith and love.

Some friends and professors from the University of São Paulo helped me to overcome obstacles on this trip. They were the ax or the hand saw needed to cut the trunks in the path. I thank especially my advisors Elcio and Filipe and my friends Alessandro, Alex, Amanda, Caio, Eveling, Gabriel, João, Jordany, Lucas, Luiza, Pablo, Raphael and Ricardo.

This study was financed in part by the Coordenação de Aperfeiçoamento de Pessoal de Nível Superior - Brasil (CAPES) - Finance Code 88887.622333/2021-00.

"Todos esses que aí estão
Atravancando meu caminho,
Eles passarão...
Eu passarinho!"
Mario Quintana

"The reward of the young scientist is the emotional thrill of being the first person in the history of the world to see something or to understand something. Nothing can compare with that experience."
Cecilia Payne-Gaposchkin

ABSTRACT

The **B**aryon Acoustic Oscillations (BAO) from **I**ntegrated **N**eutral **G**as **O**bservations (**BINGO**) radio telescope will use the neutral Hydrogen emission line to map the Universe in the redshift range $0.127 \leq z \leq 0.449$, with the main goal of probing BAO. In addition, the instrument optical design and hardware configuration support the search for **F**ast **R**adio **B**ursts (**FRBs**).

In this Master thesis, we propose the use of a **B**INGO **I**nterferometry **S**ystem (**BIS**) including new auxiliary, smaller, radio telescopes (hereafter *outriggers*). The interferometric approach makes it possible to pinpoint the FRB sources in the sky. We present here the results of several BIS configurations combining BINGO horns with and without mirrors (4 m, 5 m, and 6 m) and 5, 7, 9, or 10 for single horns.

We developed a new `Python` package, the `FRBlip`, which generates synthetic FRB mock catalogs and computes, based on a telescope model, the observed signal-to-noise ratio (S/N) that we used to compute numerically the detection rates of the telescopes and how many interferometry pairs of telescopes (*baselines*) can observe an FRB. FRBs observed by more than one baseline are the ones whose location can be determined. We thus evaluate the performance of BIS regarding FRB localization.

We found that BIS will be able to localize 23 FRBs yearly with single horn outriggers in the best configuration (using 10 outriggers of 6 m mirrors), with redshift $z \leq 0.96$; the full localization capability depends on the number and the type of the outriggers. Wider beams are best to pinpoint FRB sources because potential candidates will be observed by more baselines, while narrow beams look deep in redshift. 6 m stations, for example,

The BIS can be a powerful extension of the regular BINGO telescope, dedicated to observing hundreds of FRBs during Phase 1. Many of them will be well localized with single horn + 6 m dish as outriggers.

Keywords: Fast Radio Bursts; Radio Astronomy; Interferometry; BINGO telescope.

RESUMO

O radiotelescópio ***B**aryon Acoustic Oscillations* (BAO) *from **I**ntegrated **N**eutral **G**as **O**bservations* (**BINGO**) usará a linha de emissão de hidrogênio neutro para mapear o Universo na faixa de *redshift* $0.127 \leq z \leq 0.449$, com o objetivo principal de investigar as BAO. Além disso, o design óptico e a configuração do hardware do instrumento suportam a busca por rajadas rápidas de rádio (**FRBs**; sigla em inglês para ***F**ast **R**adio **B**ursts*).

Nesta dissertação, é proposto o uso do Sistema de Interferometria do BINGO (**BIS**; sigla em inglês para **B**INGO ***I**nterferometry **S**ystem*) incluindo novos radiotelescópios auxiliares menores (doravante chamados de *outriggers*). A abordagem interferométrica torna possível localizar as fontes de FRB no céu. Apresenta-se aqui os resultados de várias configurações do BIS combinando as cornetas do BINGO com e sem espelhos (4 m, 5 m e 6 m) e 5, 7, 9 ou 10 cornetas individuais.

Foi desenvolvido um novo pacote `Python`, o `FRBlip`, que gera catálogos sintéticos de FRB e calcula, com base em um modelo de telescópio, a razão sinal-ruído observada (S/N), usada para calcular as taxas de detecção dos telescópios e quantos pares de telescópios de interferometria (*baselines*) podem observar um FRB. FRBs observados por mais de uma *baseline* são aqueles cuja localização pode ser determinada. Avalia-se assim o desempenho do BIS em relação à localização de FRB.

Descobrimos que o BIS será capaz de localizar 23 FRBs por ano com outriggers de corneta única na melhor configuração (usando 10 outriggers de espelhos de 6 m), com redshift $z \leq 0,96$; a capacidade completa de localização depende do número e do tipo de outriggers. Feixes mais amplos são melhores para localizar fontes de FRB porque os candidatos potenciais serão observados por mais *baselines*, enquanto feixes estreitos olham profundamente no redshift. Estações de 6 m, por exemplo, são ideais para este propósito.

O BIS pode ser uma poderosa extensão do telescópio BINGO regular, dedicado a observar centenas de FRBs durante a Fase 1. Muitos deles serão bem localizados com cornetas individuais + disco de 6 m como outriggers.

Palavras-chave: *Fast Radio Bursts*; Radioastronomia; Interferometria; Telescópio BINGO.

Contents

Chapter 1

Introduction

Fast radio bursts (FRBs) are brief bursts of radio waves lasting from microseconds to milliseconds. They become dispersed as they pass through the ionized plasma of the interstellar and intergalactic medium. They were first classified as extragalactic because they were dispersed by more plasma than expected in the line-of-sight towards the source unless the source was in a high-column density environment within the Milky Way. However, it is possible that an FRB could exist within our galaxy[1]. Due to their impulsive nature and extragalactic origin, FRBs possess extraordinary brightness temperatures, making them unique radio transients. Additionally, FRBs are promising tools for studying the unseen Universe and cosmology since their signals contain information about their interactions with the intervening medium during their journey from the source to the observer. Recent reviews on this topic can be found in Katz (2018), Cordes & Chatterjee (2019), Petroff et al. (2019a), and Zhang (2022).

Only a few hundred FRBs had been detected and published up to the writing of this thesis in 2022[2] (Gal-Yam 2021), despite an expected rate of about a thousand per sky per day above modern radio telescope detection thresholds. The limited field of view and sensitivity of most radio telescopes were the main reasons for this low detection

[1]On 28 April 2020, astronomers at the CHIME telescope, reported the detection of a bright radio burst from the direction of the Galactic magnetar SGR 1935+2154 about 30,000 light-years away in the Vulpecula constellation (inside Milky-Way; Scholz & Chime/Frb Collaboration 2020).

[2]The Transient Name Server (TNS) https://www.wis-tns.org/ contains all up-to-date tally of FRBs.

rate. At the time of the first FRB discovery in 2007, using archival data from the Parkes telescope (Lorimer Burst; FRB 010724; Lorimer et al. 2007), there were no wide-field and sensitive radio telescopes suitable for FRB surveys. This led to skepticism among astronomers regarding the existence of these extragalactic radio bursts. However, in 2013, the existence of the phenomenon was confirmed in observations from the Parkes telescope, which eliminated most doubts about FRBs (Thornton et al. 2013). The discovery of the first FRB at a different site, the Arecibo observatory, in 2014, further demonstrated that the source of FRBs was not limited to the Parkes telescope (Spitler et al. 2014).

After the discovery of FRBs, instruments, and surveys were developed specifically to detect this new phenomenon. Since then, several surveys have been launched worldwide, including the UTMOST experiment (Bailes et al. 2017) in Australia, which detected its first FRB in 2016, the Commensal Real-time ASKAP Fast Transients survey (CRAFT; Macquart et al. 2010) in Australia, which detected its first FRB in 2017, on the Canadian Hydrogen Mapping Experiment (CHIME; Amiri et al. 2018) in Canada detected its first FRB in 2018 (Pleunis 2021) [3], and the Deep Synoptic Array 10-dish prototype (DSA-10; Kocz et al. 2019) in the United States, as well as the ALERT survey (van Leeuwen et al. 2023) using the new Apertif feeds on the Westerbork telescopes in the Netherlands, both of which detected their first FRBs in 2019. These are just some examples of experiments designed specifically for detecting FRBs. However, surveys at the Parkes (Australia; Champion et al. 2016), GBT (United States; Masui et al. 2015), Pushchino (Russia; Fedorova & Rodin 2019), Arecibo (Puerto Rico; Patel et al. 2018), and FAST (China; Zhu et al. 2020) telescopes have also detected FRBs after the initial discoveries mentioned above.

The first FRB discovered through the Arecibo telescope was also the first observed to repeat (Spitler et al. 2016). It has since become evident that there is a population of repeating FRB sources, and their number is growing. It is possible that all FRBs repeat

[3] See Pleunis (2021) Ph.D. thesis for a complete description of FRB detection strategies used in CHIME telescope.

but on varying time and energy scales. Moreover, the number of known catastrophic events in the universe appears insufficient to justify the rate at which FRBs are being detected, unless some or all FRB sources repeat (Ravi et al. 2019). Despite numerous observational and theoretical endeavors (Platts et al. 2019), the origin of FRBs remains elusive[4].

Brazil is also joining the field of the hunt for FRBs with the **B**aryon Acoustic Oscillations from **I**ntegrated **N**eutral **G**as **O**bservations (BINGO; Abdalla et al. 2022a). Being built originally to measure Baryon Acoustic Oscillations (BAO) through 21 cm radiation, the BINGO Collaboration is aiming to improve the telescope instruments to also detect FRBs (dos Santos et al. in prep.; see Chapter 3). This is going to substantially improve the amount and diversity of FRBs detected since BINGO is a southern sky survey, and the vast majority of the telescopes are bounded to the northern sky.

In general, surveys for FRBs and other radio transients may be designed with the aim of detecting a few transients that can be analyzed in-depth or numerous transients for population studies. This master thesis will present a simulation analysis of several possible improvements to BINGO's instruments to establish the telescope as a strong FRB detector. The upcoming sections of this chapter will give a concise overview of radio transients in general (§1.1), with a specific focus on FRBs (§1.2). The chapter concludes by presenting an outline of this thesis (§1.3).

1.1 Radio transients

1.1.1 Phase space

In the Rayleigh-Jeans limit of the Planck distribution, radio transients can be parameterized based on the burst or pulse width, W, and the pseudo-luminosity, $S_\nu d_\mathrm{A}^2$, of a source with brightness temperature, T_B. This relationship is given by

[4]An overview of FRB models is summarized and regularly updated at https://frbtheorycat.org/.

$$T_{\rm B} = \frac{1}{2\pi k_{\rm B}} \frac{S_\nu d_{\rm L}^2}{(\nu W)^2}\,, \tag{1.1}$$

where S_ν is the observed flux density for a given emission frequency ν, $d_{\rm L}$ is the luminosity distance, and $k_{\rm B}$ is Boltzmann's constant. Cordes et al. (2004), Keane (2010) and Zhang (2020) have shown that this equation forms a phase space of radio transients in terms of their $S_\nu d_{\rm L}^2$ and νW, as depicted in Fig. 1.1. The νW parameter is introduced by expressing the size of the emitting region as the light travel time in a causally connected region. FRBs are a remarkable class of sources in this space as they are the most luminous short-duration transients currently known.

The emission mechanism responsible for FRBs must be non-thermal and coherent since their brightness temperature $T_{\rm B}$ exceeds 10^{12} K. This temperature limit is due to the inverse Compton cooling of relativistic electrons, as noted by Kellermann & Pauliny-Toth (1969). To avoid causality violations, the emitting area of any transient must be smaller than the light travel time cW, which means the FRB emitting region must be less than 300 km for 1-ms bursts and 3 km for 10-μs bursts, disregarding geometric and/or relativistic effects. However, if the emitting region R is moving towards the observer with a Lorentz factor γ, the observer sees a smaller region of R/γ, and the constraint on the emitting region becomes less strict.

Electrically charged particles emit non-thermal electromagnetic waves when they are accelerated, either incoherently or coherently. The total power emitted is proportional to the number of particles, n, and to n^2 for incoherent and coherent processes, respectively. Consequently, coherent emission processes can achieve higher effective $T_{\rm B}$ than incoherent processes. As can be seen in Fig. 1.1 there are multiple classes of radio transients that emit coherently.

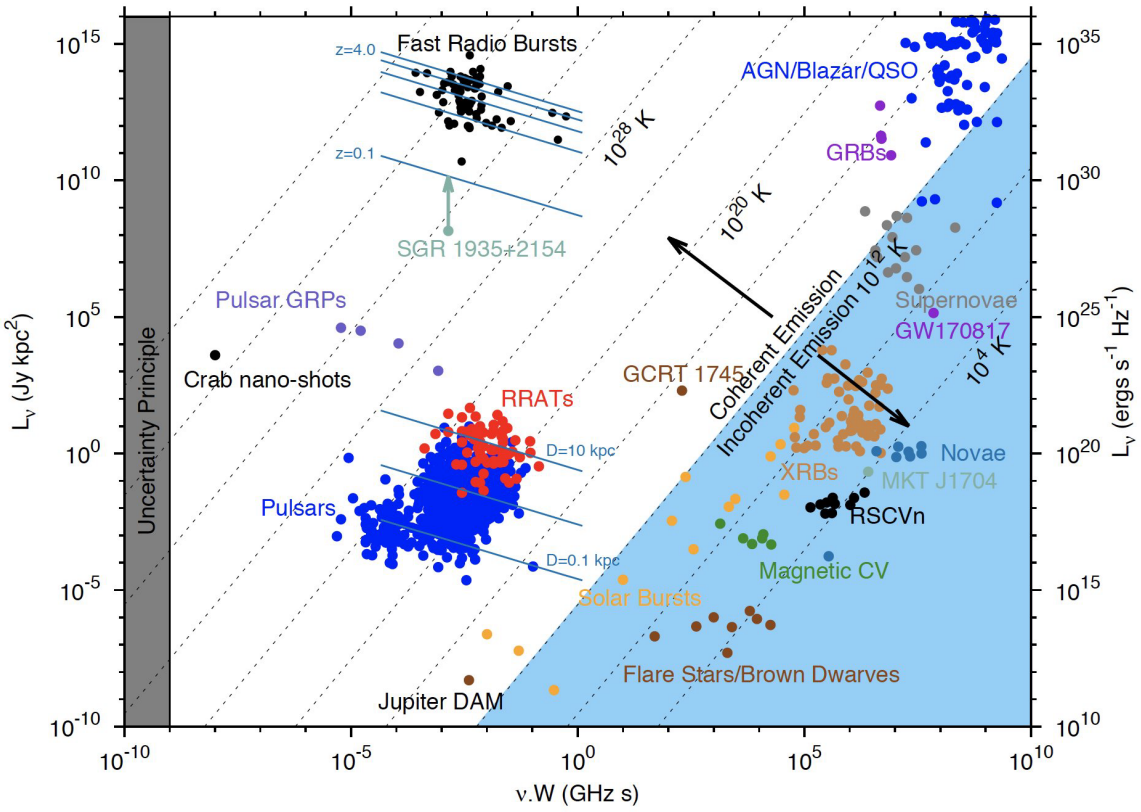

Figure 1.1: The plot depicts the phase space of radio transients, with pseudo-luminosity on the y-axis and the product of emission frequency and burst width on the x-axis. Diagonal dashed lines indicate constant effective brightness temperature, with $T_{\rm B} \approx 10^{12}$ K roughly distinguishing incoherent and coherent emission processes (as explained in the main text). FRBs are notably distinct from other radio transients in terms of their luminosity. A noticeable gap in the phase space between Galactic pulsars and RRATs and extragalactic FRBs has recently been bridged by the detection of a bright radio burst from the Galactic magnetar SGR 1935+2154. The figure was created by Keane (2018).

1.1.2 Propagation effects

As radio signals travel through space, they interact with the plasma that fills the interstellar medium (ISM) of the Milky Way. Although the ISM is almost a vacuum, it contains a small number of free electrons, resulting in a non-zero current density (indeed, their mean density $n_e \approx 0.03$ cm^{-3}; Draine 2010). These electrons affect the velocity of the radio waves, causing lower frequencies to arrive later than higher ones. Despite the small electron density, this effect can be measured because of the long distances that the waves travel. Additionally, the presence of magnetic fields causes a difference in the phase velocity of right- and left-circularly polarized radio waves, resulting in a Faraday rotation of the plane of polarization of linearly polarized radio waves. Inhomogeneities in the plasma also lead to scintillation and scattering of the radio waves. The study of these effects provides valuable information about the density structure of the ISM (Cordes & Chatterjee 2019).

Dispersion

The electrons in the ISM make up a cold plasma with a refractive index

$$\mu = \left[1 - \left(\frac{\nu_p}{\nu}\right)^2\right]^{1/2}, \tag{1.2}$$

where ν is the frequency of the radio waves and ν_p is the plasma frequency. The plasma frequency is given by[5]

$$\nu_p = \sqrt{\frac{e^2 n_e}{m_e \epsilon_0}}, \tag{1.3}$$

where n_e is the number density of electrons, e is the electric charge, m_e is the effective mass of the electron, and ϵ_0 is the permittivity of free space.

Within the ISM, $n_e \approx 0.03$ cm^{-3}, therefore, $\nu_p \approx 1.5$ kHz. Radio waves cannot travel through the ISM if their frequency ν is lower than the plasma frequency ν_p. The group velocity of the waves that can propagate is μc, where μ is less than 1, and c

[5]Note that the above formula is derived under the approximation that the ion mass is infinite. This is generally a good approximation, as the electrons are so much lighter than ions.

is the speed of light. As a result, there is a frequency-dependent dispersion delay in the arrival time Δt of the waves. Upon observing between two frequencies, ν_1 and ν_2 (where ν is much greater than ν_p), such a delay occurs. This is the case for FRBs, since according to the TNS catalog, the vast majority were detected between 800 MHz and 8 GHz (much larger than $\nu_\mathrm{p} \approx 1.5$ kHz). The delay Δt is given by

$$\Delta t = k_\mathrm{DM}\,\mathrm{DM}\,\left(\nu_1^{-2} - \nu_2^{-2}\right)\ \mathrm{ms}\ , \tag{1.4}$$

where ν_1 and ν_2 are used in MHz and DM is the dispersion measure given in pc cm^{-3}. The dispersion measure is the integrated column density of free electrons between the source and the observer, that is

$$\mathrm{DM} = \int_0^d n_\mathrm{e}\,\mathrm{d}\ell\,, \tag{1.5}$$

where d is the distance through the plasma and n_e the free electron density. The definition of the constant k_DM is

$$k_\mathrm{DM} = \frac{1}{8\pi^2}\frac{e^2}{\epsilon_0 m_\mathrm{e} c} \times\ \mathrm{parsec} \approx 4149.38\ \mathrm{GHz}^2\ \mathrm{cm}^3\ \mathrm{pc}^{-1}\ \mathrm{s}\ . \tag{1.6}$$

The dispersion measure DM is not only affected by free electrons but also by ions and is sensitive to the plasma temperature, meaning that it is not strictly related to only the column density of free electrons (although the additional effects are negligible).

The observed DM is the total sum of all the line integrals of ionized plasma that a burst encountered,

$$\mathrm{DM}_\mathrm{obs} = \mathrm{DM}_\mathrm{MW} + \mathrm{DM}_\mathrm{MW,halo} + \mathrm{DM}_\mathrm{cosmic}(z) + \mathrm{DM}_\mathrm{host}\,, \tag{1.7}$$

where DM_MW and $\mathrm{DM}_\mathrm{MW,halo}$ are the contributions from the ISM and halo of the Milky Way, $\mathrm{DM}_\mathrm{cosmic}(z)$ is the contribution from the intergalactic medium (IGM) in the redshift z, and $\mathrm{DM}_\mathrm{host}$ is the contribution from the interstellar medium and halo

from the host galaxy of a source. It is possible to break down $\mathrm{DM_{host}}$ into a galaxy and halo component, and an additional DM component may be present due to interactions with intervening galaxies or halos in the IGM.

FRBs are defined by their DMs exceeding the contribution from our Galaxy along their lines of sight. Therefore, distinguishing between FRBs and bursts or pulses from Galactic RRATs or pulsars requires a thorough understanding of the Galactic DM contribution (Keane et al. 2016). Two available models for the distribution of free electrons in our Galaxy are NE2001 (Cordes & Lazio 2002) and YMW16 (Yao et al. 2017), which are based on modeling various Galaxy components and are calibrated to pulsars with independently measured distances.

The estimates for $\mathrm{DM_{MW,halo}}$ vary significantly, ranging from a few units to approximately 50 pc $\mathrm{cm^{-3}}$, as reported by Prochaska & Zheng (2019a), Keating & Pen (2020), and Platts et al. (2020). To determine $\mathrm{DM_{cosmic}}(z)$, assumptions must be made regarding the ionization fractions of the baryons in the IGM and the electron-to-baryon fraction (Ioka 2003; Inoue 2004; Zhang 2018a). The Macquart relation, or DM-z relation, has been measured for the first time using a sample of well-localized ASKAP FRBs (Macquart et al. 2020b). A useful approximation is $\mathrm{DM_{cosmic}}(z) \approx 1000\,z$ pc $\mathrm{cm^{-3}}$. The value of $\mathrm{DM_{host}}$ depends heavily on the host galaxy's type and its viewing angle relative to Earth, meaning that if the FRB travels through a face-on galaxy, it will likely encounter less material than if it passes through an edge-on galaxy.

1.2 Fast radio bursts

The fundamental characteristics of FRBs were established following the discovery of the first burst (Lorimer et al. 2007). FRBs are observable as transient events lasting approximately a few milliseconds from distances around a few billion parsecs. This indicates that they possess extremely high brightness temperatures of around $\sim 10^{36}$ K, release vast amounts of energy of about $\sim 10^{33}$ J, and originate from compact objects with a size $\lesssim 10^3$ km. These features suggest that FRBs arise from coherent emission.

Contemporary radio telescopes can detect about one thousand FRBs per day above their sensitivity threshold of a few Jy ms. Initial attempts to explain the origin of FRBs were mostly theoretical, involving speculative scenarios that could satisfy these broad constraints.

The discovery of a repeating source of FRBs revealed another important property (Spitler et al. 2016). This finding prompted the classification of FRBs into two categories: one-off bursts and repeaters. Although some FRBs have been observed for hundreds of hours without any signs of repetition, it is not yet clear if all FRBs repeat at different times and energy scales. The non-repeating bursts are sometimes referred to as apparent non-repeaters or so-far-non-repeaters. The existence of at least some FRB sources that repeat has led to a surge of general models that meet the previously established constraints without being cataclysmic, which means they do not destroy the FRB production site in the process (see §1.2.3 below).

There are many hypothesized progenitors of FRBs that have been proposed, and we have access to numerous additional observables beyond the order-of-magnitude constraints. These observables can help in falsifying each of the proposed models until only one or a few remain viable. However, it's important to keep expectations in check, for instance: we still do not fully understand why pulsars emit radiation, despite more than fifty years of research since their discovery.

1.2.1 Observables

What follows is a list of observables for individual FRBs and their most common units, with observed ranges of values from https://www.wis-tns.org/ (Gal-Yam 2021) unless other citations are provided.

- **Dispersion measure DM [pc cm^{-3}]:** As defined in §1.1.2, the DM of an FRB is determined by optimizing the dispersion delay correction of the burst. This is typically achieved by testing a range of trial DMs and selecting the DM that maximizes the signal-to-noise ratio or burst structure. Currently, FRBs have

been observed with DMs of up to approximately 3000 pc cm^{-3}.

- **Burst width [ms]:** This is measured as either the observed or intrinsic (modeled) width. The intrinsic width is broadened due to propagation effects such as dispersion smearing and scattering. The width serves as a crucial constraint on potential progenitors and emission mechanisms.

- **Dispersion index:** The dispersion delay of a cold and tenuous plasma $\propto \nu^{-2}$ (cf. Eq. (1.4), and any deviations from the -2 index point to additional dispersive effects either at the source or in the intervening plasma. The dispersion index can be constrained by fitting a delay $\propto \nu^{\alpha}$ to a burst. No significant deviations have been observed so far.

- **Scattering timescale [ms]:** The plasma in which the pulsar travels contains irregularities that result in the multi-path propagation of FRBs. This phenomenon leads to scattering tails that resemble exponential functions. The impact of this effect varies significantly with frequency, typically following a $\propto \nu^{-4}$ relationship. By measuring the burst width at various frequencies, researchers can deduce information about the environment that the FRB has traversed.

- **Scattering index:** by adjusting the scattering timescale index, which is typical $\propto \nu^{-4}$, researchers can gain insight into how the inhomogeneities in the plasma scale contribute to the scattering effect. For pulsars observed at around 150 MHz using LOFAR, the measured scattering indices range from -1.5 to -4, as reported by Geyer et al. (2017). Meanwhile, for the few FRBs where indices are available (though somewhat imprecise), the range spans approximately -2.5 to -6.

- **Flux [Jy $= 10^{-26}$ W m^{-2} Hz^{-1}]:** The peak intensity of an FRB serves as a benchmark for the amount of energy that any proposed theoretical model must account for. These bursts exhibit fluxes ranging from $\mathcal{O}(10^{-2})$ to $\mathcal{O}(10^{2})$ Jy, but because the exact sky locations of most FRBs are not well-defined, flux

measurements are typically lower limits. This is because they assume the FRB was detected at the center of the telescope's beam, rather than accounting for the sensitivity of the beam towards the FRB's (uncertain) position in the sky.

- **Fluence [Jy ms]**: The total energy released during an FRB event provides a comprehensive energy scale that any theoretical model must account for. These events typically exhibit integrated fluxes ranging from $\mathcal{O}(10^{-1})$ to $\mathcal{O}(10^{2})$ Jy ms. However, it's worth noting that most of these values represent lower limits, just like flux measurements, since the precise sky position of many FRBs is not yet known.

- **Spectrum:** This refers to the scope and shape of FRB spectra. FRBs have been observed at frequencies ranging from 300 MHz (Chawla et al. 2020) to 8 GHz (Gajjar et al. 2018a). Typically, the spectra of bursts that span the full bandwidth of a receiver are characterized by a power-law function $\propto \nu^{\alpha}$, where α is the spectral index. In the case of ASKAP bursts, their mean and median spectra appear to be well-fit by a power law with an index of -1.6 or -1.4, respectively (Macquart et al. 2019a). For narrower-band bursts, the spectral extent is commonly defined as the burst bandwidth's full width at half-maximum (FWHM) or full width at tenth-maximum (FWTM). In addition to the broad structure of FRB spectra, finer-scale structures such as intensity modulation caused by scintillation (e.g., Masui et al. (2015)) and fine structures that may be due to the emission process (Farah et al. (2018); Shannon et al. (2018)) are observed. Furthermore, some FRBs consist of multiple sub-bursts that occasionally drift down in frequency as time passes (see next item). Spectral characteristics like those described here provide insight into emission mechanisms and propagation effects.

- **Drift rate [MHz ms^{-1}]:** The rate at which sub-bursts shift towards lower frequencies in the "sad trombone" bursts is of particular interest. Typically, this drift is assumed to be linear and can be calculated by fitting a linear slope

through the centroids of the sub-bursts or through the autocorrelation of the burst dynamic spectrum. Measured drift rates range from a few to tens of MHz ms^{-1} around 600 MHz up to almost a GHz ms^{-1} around 6.5 GHz (Caleb et al. 2020). The drifting phenomenon, as well as the observed drift rates, must be accounted for by an emission mechanism or a propagation effect.

- **Rotation measure [rad m^{-2}]:** RM, which was defined in §1.1.2, is measured by fitting burst polarization as a function of wavelength for a range of possible RM values and determining the best-fit value. The majority of observed FRB RMs range from a few tens to a few hundreds of rad m^{-2}. However, for FRB 121102, the RM was as high as 10^5 rad m^{-2}, but it has since decreased (Michilli et al. 2018).

- **Linear polarization fraction:** For many FRBs, the degree of linear polarization has been observed to be near or at 100%. This provides a strong limitation on the possible FRB emission mechanisms.

- **Position angle evolution:** The variation of the position angle (PA) of FRBs with respect to individual bursts can offer valuable information regarding the emission mechanism of FRBs. In some cases, the PAs remain constant, while in others, they exhibit a swing-like pattern resembling the shape of the letter "S". The latter indicates that the emission may originate from a rotating object, as seen in pulsars (Radhakrishnan & Cooke 1969; Manchester et al. 1975). On the other hand, a flat PA curve could imply a wide emission cone or emission that is not associated with rotation.

- **Redshift:** Can be estimated from $\mathrm{DM}_{\mathrm{cosmic}}(z)$ by the Macquart relation (see §1.1.2) or it can be measured by identifying spectral lines in the spectrum of the host galaxy associated with the FRB.

- **Sky position:** Accurate determination can result in an association with a host galaxy. However, for a clear and definitive association, detection using an

interferometer with extremely long baselines is typically required (more on this in §3).

- **Multi-wavelength counterparts:** If an electromagnetic, astroparticle, or gravitational wave detection occurs simultaneously and in the same location as an FRB, it can offer valuable insights into the origin of the FRB source.

For repeating sources of FRBs this list is further extended.

- **Repeat rate:** The number of bursts observed above a certain sensitivity threshold per unit of time is known as the repeat rate, which may vary depending on the frequency. This rate serves as a useful metric for scheduling follow-up observations and also acts as a constraint on repeater models.

- **Wait time:** The typical time between subsequent bursts informs models for repeaters.

- **Energy distribution:** The way in which the number of bursts with a particular energy is spread out can reveal valuable insights about progenitor models, while the ratio of brighter to dimmer events can guide decisions on follow-up observation approaches.

- **Periodicity:** If the arrival times of bursts exhibit a consistent and precise pattern, it indicates that the FRB-producing (compact) object is rotating. Alternatively, the sources may display periodic behaviors with intermittent bursts, suggesting that some binary interaction is causing the FRBs or that the presence of intrabinary material is either enhancing (e.g., via plasma lensing) or hindering (e.g., via absorption) the FRB emission. These longer timescale periodicities may point to orbital motion.

Then, for the full population, the important observables are as follows.

- **Sky distribution:** The distribution of FRBs across the sky can provide insight into their isotropic distribution across the cosmos, their adherence to large-scale

structure (as demonstrated by Rafiei-Ravandi et al. 2020), and the potential influence of Galactic latitude on their detection (as explored by Petroff et al. 2014).

- **Redshift distribution:** Such analysis can aid in identifying the cosmological population responsible for generating FRBs. For instance, if the frequency of FRBs aligns with the documented history of star formation in the cosmos (as suggested by Niino 2018), it can offer clues regarding the FRBs' source.
- **Volumetric distribution:** The sky and redshift distribution of FRBs can enable the calculation of the frequency of FRBs per unit volume. This information can then be utilized to restrict progenitor models (as demonstrated by Ravi 2019b). For instance, if a hypothesis posits core-collapse supernovae (CCSNe) as the source of FRBs, the number of CCSNe occurring in a given volume must correspond to the deduced rate of FRBs.
- **Dispersion measure distribution:** In addition to its correlation with the redshift distribution of FRBs (via the Macquart dispersion measure-redshift relation), the dispersion measure distribution presents an opportunity for identifying the epoch of helium reionization, given the detection of numerous FRBs within the $3 < z < 5$ range (Macquart & Ekers 2018; Caleb et al. 2019; Linder 2020).

1.2.2 Host Galaxies

Establishing the connection between an FRB and its host galaxy not only offers insight into its redshift but also facilitates the identification of FRB progenitors, as certain progenitor types may be more prevalent in specific galaxy types. However, the precision of this association is dependent on factors such as the localization uncertainty region, DM/redshift, and the brightness of galaxies within the localization region. As redshift increases, there is greater ambiguity within a given sky area, and the likelihood of discovering a brighter galaxy in that area is reduced compared to that of a fainter galaxy (Eftekhari & Berger 2017).

By achieving sub-arcsecond localization for nine of the roughly 110 published FRBs, the identification of their host galaxies has verified their cosmological origin, placing them at redshifts ranging from 0.03 to 0.66 (Chatterjee et al. 2017; Bannister et al. 2019; Ravi 2019a; Prochaska & Zheng 2019b; Marcote et al. 2020; Macquart et al. 2020a). Host galaxies of one-off FRBs vary from star-forming spiral galaxies (e.g., FRB 190608, as reported by Chittidi et al. (2021)) to early-type spirals (e.g., FRB 180924, as documented by Bannister et al. (2019)). The first localized repeater, FRB 121102, is situated within an irregular, low-metallicity dwarf galaxy, linking it to known hosts of superluminous supernovae (SLSNe, per Bassa et al. (2017)). However, the second repeater is situated in the star-forming region of a massive spiral galaxy (Marcote et al. 2020).

According to Bhandari et al. (2020), a comparison of host galaxies of FRBs reveals that those localized by ASKAP are usually situated at the edges of their host galaxies, effectively ruling out progenitor models involving active galactic nuclei. Furthermore, the stellar populations of the hosts of ASKAP FRBs are dissimilar to those of FRB 121102, thereby making it improbable that those FRBs are also associated with remnants of SLSNe.

The small sample size of host galaxies for both one-off and repeater FRBs demonstrates a range of diversity, indicating a distinction between the two categories. Nevertheless, to establish definitive conclusions, further associations are essential given the limited number of observations.

1.2.3 Possible progenitors

Astronomers are actively seeking to identify the sources of FRBs, determine their energy sources, and understand how they form. In order to develop a viable FRB progenitor model, it must be capable of explaining the observed burst characteristics, such as their duration (ranging from a few tens of microseconds to a few milliseconds), energetics (up to approximately 10^{43} erg s^{-1} for isotropic emission), and a burst rate of around 1.7×10^3 FRBs per sky per day above a flux density of approximately 2 Jy

(Bhandari et al. 2018). The goal is to develop a comprehensive understanding of the nature of FRBs and the mechanisms that drive them.

To develop a viable FRB progenitor model, it is crucial to consider the dynamical time scales that match observed burst durations, as argued by Lu & Kumar (2018). If the FRB is believed to originate from a stellar collapse or accretion event, then the free-fall time $t_{\rm ff} \sim (R^3/GM)^{1/2}$ governed by gravity, for an object of radius R and mass M, is a relevant timescale. For a neutron star (NS) or black hole (BH; $R_{\rm Schwarzschild} = 2MG/c^2$), with typical values of $M \approx 1.4{\rm M}\odot$ and $R \approx 10$ km, the free-fall time is approximate ~ 0.1 ms. On the other hand, for a white dwarf (WD) with $M \approx {\rm M}\odot$ and $R \approx 7000$ km, the free-fall time is much longer at ~ 10 s. Therefore, any model involving dynamics around a WD is less likely. In the case of accretion from a disk, the relevant timescale is the viscous timescale $t_{\rm vis} \sim \rho R^2/\bar{\eta}$, where ρ is the density and $\bar{\eta}$ is the average shear viscosity in the disk. However, this timescale is typically much longer than the free-fall timescale.

The light crossing time of an emitting region with size R is what links causality to the minimum burst duration, which can be expressed as $R/c \sim 30(R/10^9$ cm) ms. This constraint disfavors the possibility of WD as progenitors unless the emission is confined to a smaller region on the surface or in the magnetosphere of the WD. However, the constraint can be relaxed by a factor of $\sim 2\gamma^2$ when the emitting plasma is moving relativistically towards the observer with a Lorentz factor $\gamma \gg 1$. Such plasma can only be launched by a neutron star or black hole. Therefore, based on burst duration considerations alone, it is difficult to imagine any other progenitor than an NS or BH (Katz 2018).

Possible progenitor models can be categorized into two groups: cataclysmic models, which are ruled out for repeating FRBs, and models that allow for repetition. The latter group can be further subdivided into compact object models and exotic models. Within the compact object models, there are three subcategories: pulsar-like models, which rely on tapping into the rotational energy of the compact object; magnetar-like models, which rely on tapping into the magnetostatic energy of the compact object;

and interaction models, which rely on energy extraction from the interaction with a binary companion or a nearby object that is not necessarily gravitationally bound to the compact object.

Pulsar-like progenitors

According to Lorimer et al. (2005), the spin-down luminosity $L_{\rm sd}$ of an NS and its rate of rotational energy loss is $\propto P^{-3}\dot{P}$, where P is the spin period and $\dot{P}$ is the spin period derivative. In order to account for the energetics of FRBs, a pulsar must have a fast spin period ($\lesssim 10$ ms) and be spinning down rapidly. As a result, young pulsars ($\lesssim 1000$ yrs) with Crab-like giant pulses are the most likely candidates for FRBs (Cordes & Wasserman 2016; Lyutikov et al. 2016; Munoz et al. 2020). The supernova remnant (SNeR) left over from the pulsar's explosion is expected to be opaque to FRB emission for approximately the first 10 years, but the pulsar's embedding in the SNR at later times could explain observed RM values in the 100-1000 rad m^{-2} range (Connor et al. 2016). If a strict periodicity is detected in the arrival times of bursts and/or the DM/RM evolution of sources matches those calculated from models of SNeRs (Piro & Gaensler 2018), these models will gain more credibility.

Magnetar-like progenitors

The large magnetic energy reservoir of magnetars makes them a feasible origin for FRBs, as supported by Kaspi & Beloborodov (2017). Additionally, the association of FRBs 121102, 180916.J0158+65, and 190608 with star-forming regions in their host galaxies (where short-lived magnetars are located), along with a magnetar birth rate that matches the observed FRB rate (Nicholl et al. 2017) and the recent detection of a bright radio burst from the Galactic magnetar SGR 1935+2154 (Lu et al. 2020; Margalit et al. 2020), further support this link. Many models have been proposed in which FRBs are generated from the flaring activity of magnetars (Popov & Postnov 2013; Kulkarni et al. 2014; Lyubarsky 2014; Katz 2016; Beloborodov 2017; Kumar et al. 2017; Metzger et al. 2017; Margalit & Metzger 2018). These models suggest that

the FRBs either originate near the magnetosphere of the neutron star or further out, with various emission mechanisms proposed (for a clear overview of different magnetar models for FRBs, see Margalit et al. 2020).

Interaction models

Several models propose that single or repeating FRBs can be created by the catastrophic or repetitive interaction of two objects. For instance, the merger of two WDs (Kashiyama et al. 2013), two NSs (Totani 2013), two BHs (Zhang 2016), a BH and an NS (using a "black hole battery"; Mingarelli et al. 2015) could provide the necessary energy and conditions to generate FRBs for a brief period or accretion events between NSs and WDs have been proposed (Gu et al. 2016) as a more extended FRBs generator.

An alternative approach to generating repeating FRBs involves the interaction between a pulsar and a smaller celestial body, such as a planet, asteroid, or white dwarf. These systems can produce repeating FRBs in a stable burst-generating configuration or through repeated interactions with an asteroid belt, for example. Models focusing on asteroids have received significant attention from researchers (Geng & Huang 2015; Dai et al. 2016; Bagchi 2017). A more energetically favorable approach to generating FRBs is through the interaction between a pulsar and a plasma stream from a nearby source, such as an AGN, a GRB, or a supernova (Zhang 2017, 2018b).

1.2.4 Possible emission mechanisms

In order to be a viable model for FRB emission, the mechanism must account for the observed radio luminosity, spectra, and polarization of the bursts, as described in §1.2. Additionally, the model must be connected to a progenitor model that can supply the required energy and magnetic field to drive the emission. Since FRBs are commonly detected at GHz frequencies, the emission mechanism must peak around this frequency range.

As previously mentioned, the observed brightness temperature of FRBs exceeds the maximum temperature of a blackbody, which implies that FRB emission must be

non-thermal. This means that the emission process does not depend on temperature and can be either incoherent or coherent. In the case of incoherent emission, the radiated power is proportional to the number of particles (n) and the power per particle (P_{single}), while in the case of coherent emission, the radiated power is proportional to the square of the number of particles (n^2) and the power per particle (P_{single}). To account for the high brightness temperatures observed in FRBs, a coherent emission process is necessary.

Several coherent emission mechanisms were developed to explain pulsar emission, including antennas, reactive, and maser instabilities. A review by Melrose (2017) covers these mechanisms. As for FRBs, curvature radiation and synchrotron maser emission appear to be possible mechanisms, as suggested by studies by Cordes & Wasserman (2016), Kumar et al. (2017), Ghisellini, Gabriele & Locatelli, Nicola (2018), Lu & Kumar (2018), Waxman (2017), Gruzinov & Levin (2019), Metzger et al. (2019), Beloborodov (2020). However, detailed simulations, such as those conducted by Plotnikov & Sironi (2019), will be necessary to determine the feasibility of any emission mechanism.

1.3 Outline of thesis

It is evident that a multitude of significant inquiries surrounding FRBs remains unresolved. These include but are not limited to, the repetition of all FRBs, the presence of multiple classes of FRBs, the progenitor responsible for FRB emission, and the underlying mechanism driving the FRB phenomenon. In an effort to shed light on these and other critical questions, the BINGO telescope experiment has been developed with the objective of detecting a large number of FRBs.

In this Master's thesis, I investigated the performance of the BINGO telescope in detecting FRBs. Additionally, the feasibility of using a set of outriggers to localize the FRBs in the sky through the BINGO Interferometric System (BIS) was explored. The investigation involved evaluating the detection capabilities of a single, naked horn as

well as three different mirror sizes for the outriggers. Specifically, the study considered 5, 7, 9, and 10 outriggers, each equipped with a single horn. To generate synthetic FRBs and calculate detection rates, I used and helped to develop the code `FRBlip`, reaching $\sim$ 180 localized FRBs by at least 3 baselines with redshifts up to 1.3.

Using various techniques for defining detection and localization through baselines, it has been estimated that the BINGO telescope alone will be capable of observing dozens of Fast FRBs per year. Specifically, around 50 FRBs with a signal-to-noise ratio (S/N) of at least 5 and 20 with S/N of at least 15 (in certain circumstances to be discussed) can be detected, which is consistent with prior calculations presented in Abdalla et al. (2022a). The inclusion of outriggers can improve the overall detection rate by approximately 20% with 9 outriggers.

The remainder of this thesis is organized as follows: Chapter 2 is a review of basic radio astronomy with concepts and definitions that are going to be used in the whole thesis; Chapter 3 describes the BINGO telescope and in particular presents the BINGO Interferometry System with and corresponding simulations; Chapter 4 I present the different outrigger configurations, compare their performances, and discuss the different criteria to define the detection and localization of an FRB; Chapter 5 is reserved for conclusions including some directions for future research and other contributions I have participated in these two years of work.

Chapter 2

Radio Astronomy Basics

This chapter reviews the necessary concepts of radio astronomy that will be used in the whole thesis, especially the assumptions made to model the BINGO telescope and to create the FRB mocks. The description presented here is based on Rohlfs & Wilson (2013).

2.1 Basic definitions

The electromagnetic radiation in the radio window is a wave phenomenon. The BINGO radio window is from 23.79 cm to 30.59 cm and its main and secondary diameters are respectively 40.0 m and 35.6 m (more on this in Chapter 3). Since the scale of the system is much larger than the wavelength, we can consider the radiation to travel in straight lines called rays. This is common to a vast majority of radio telescopes.

2.1.1 Brightness and flux density

We start by establishing the definition of the brightness I_ν (also known as intensity or specific intensity), that is (see Fig. 2.1)

$$\mathrm{d}P \;=\; I_\nu \,\cos\theta\,\mathrm{d}\Omega\,\mathrm{d}\sigma\,\mathrm{d}\nu\,, \tag{2.1}$$

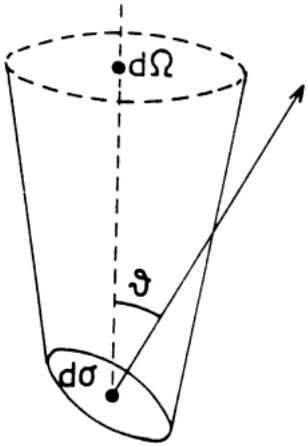

Figure 2.1: A sketch to illustrate the definition of brightness.

where $\mathrm{d}P$, $\mathrm{d}\sigma$, $\mathrm{d}\nu$, $\mathrm{d}\Omega$ and θ are respectively the infinitesimal power in watts, infinitesimal area of the surface in cm^2, infinitesimal bandwidth in Hz, infinitesimal solid angle element and the angle between the normal to $\mathrm{d}\sigma$ and the direction to $\mathrm{d}\Omega$. The units of I_ν is W m^{-2} Hz^{-1} sr^{-1}.

We can obtain the total flux density of a source by integrating (2.1) over the total solid angle Ω_s subtended by the source as

$$S_\nu = \int\limits_{\Omega_s} I_\nu(\theta, \varphi) \cos\theta \, \mathrm{d}\Omega \,. \tag{2.2}$$

The flux density is measured in units of W m^{-2} Hz^{-1}. It is quite often to write the flux in Jansky (Jy) units, where 1 Jy $= 10^{-26}$ W m^{-2} Hz^{-1} $= 10^{-26}$ erg s^{-1} cm^{-2} Hz^{-1}. This is done because the flux density of radio sources is usually very small, rarely being as bright as 1 Jy.

Now we consider a sphere with uniform brightness I_ν with radius R (see Fig. 2.2). The total flux density received by an observer at the distance r then is, according to (2.2),

$$S_\nu = \int\limits_{\Omega_s} I_\nu \cos\theta \, \mathrm{d}\Omega = I_\nu \int\limits_0^{2\pi} \int\limits_0^{\theta_\mathrm{c}} \sin\theta \cos\theta \, \mathrm{d}\theta \, \mathrm{d}\varphi \,, \tag{2.3}$$

where

$$\sin\theta_c \;=\; \frac{R}{r} \tag{2.4}$$

defines the angle θ_c that the radius of the sphere subtends at r. We obtain

$$S_\nu \;=\; \pi\, I_\nu\, \sin^2\theta_c\,, \tag{2.5}$$

or

$$S_\nu \;=\; I_\nu\, \frac{\pi R^2}{r^2} \;=\; I_\nu\, \Delta\Omega\,, \tag{2.6}$$

where $\Delta\Omega$ is defined as the area subtended by an object at a distance r. Of course, the total flux density, S_ν, shows the expected dependence of $1/r^2$.

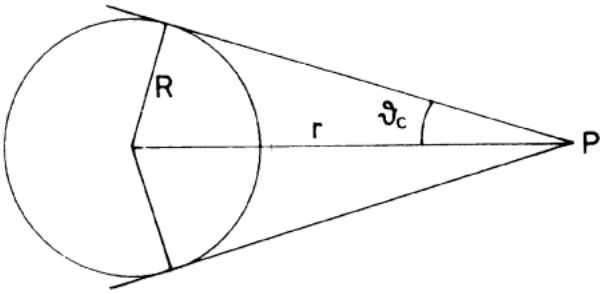

Figure 2.2: Total flux received at a point P from a uniformly bright sphere.

2.1.2 Radiative transfer

The brightness is a property of the source. In free space, I_ν remains independent of the distance along a ray. It will change only if radiation is absorbed or emitted. This change of I_ν is described by the equation of transfer. Let us adopt a macroscopic approach here. For a change in I_ν along the line of sight, a loss term $\mathrm{d}I_{\nu-}$ and a gain $\mathrm{d}I_{\nu+}$ are introduced, and we adopt the form

$$\mathrm{d}I_{\nu-} \;=\; -\kappa_\nu\, I_\nu\, \mathrm{d}s\,, \tag{2.7}$$

$$\mathrm{d}I_{\nu+} \;=\; \varepsilon_\nu \mathrm{d}s\,, \tag{2.8}$$

where κ_ν and ε_ν are, respectively, the linear absorption and the emission coefficients. The change in a slab of material of the thickness $\mathrm{d}s$ is

$$[I_\nu(s+\mathrm{d}s) \;-\; I_\nu(s)]\;\mathrm{d}\sigma\,\mathrm{d}\Omega\,\mathrm{d}\nu \;=\; [-\kappa_\nu\, I_\nu + \varepsilon_\nu]\;\mathrm{d}\sigma\,\mathrm{d}\Omega\,\mathrm{d}\nu\,, \tag{2.9}$$

resulting in the equation of transfer

$$\frac{\mathrm{d}I_\nu}{\mathrm{d}s} = -\kappa_\nu\, I_\nu + \varepsilon_\nu\,. \tag{2.10}$$

There are several limiting cases for which the solution of the differential equation (2.10) is especially simple. We are interested in the thermodynamic equilibrium situation. If the radiation is in complete equilibrium with its surroundings, the temperature T totally describes the brightness distribution through the Planck function, that is

$$\frac{\mathrm{d}I_\nu}{\mathrm{d}s} = 0\,, \qquad\qquad I_\nu = B_\nu(T) = \frac{\varepsilon_\nu}{\kappa_\nu}\,, \tag{2.11}$$

$$B_\nu(T) = \frac{2h\nu^3}{c^2}\frac{1}{\mathrm{e}^{h\nu/k_\mathrm{B}T}-1}\,. \tag{2.12}$$

where h, c, and k_B stand for respectively the Planck's constant, the speed of light in vacuum, and the Boltzmann constant.

2.1.3 Brightness temperature

The Eq. (2.12) gives us the spectral distribution of the radiation of a black body in thermodynamic equilibrium. Let us integrate (2.12) with respect to the frequency ν to obtain the total brightness $B(T)$ of a black body,

$$B(T) = \frac{2h}{c^2}\int_0^\infty \frac{\nu^3}{\mathrm{e}^{h\nu/k_\mathrm{B}T}-1}\,\mathrm{d}\nu\,. \tag{2.13}$$

Substituting

$$x = \frac{h\nu}{k_{\rm B}T}\,, \tag{2.14}$$

we get

$$B(T) = \frac{2h}{c^2}\left(\frac{k_{\rm B}T}{h}\right)^4 \int_0^\infty \frac{x^3}{{\rm e}^x - 1}\,{\rm d}x\,. \tag{2.15}$$

This integral amounts to $\pi^4/15$. Thus,

$$B(T) = \sigma T^4\,, \qquad \sigma = \frac{2\pi^4 k_{\rm B}^4}{15c^2h^3} = 1.8047\times10^{-5}\ {\rm erg\ cm^{-2}\,s^{-1}\,K^{-4}}\,, \tag{2.16}$$

which is the Stefan-Boltzmann law.

The frequency that maximizes the distribution in (2.12) can be easily found by doing $\partial B_\nu/\partial\nu = 0$

$$\frac{2h}{c^2}\frac{\partial}{\partial\nu}\left(\frac{\nu^3}{{\rm e}^{h\nu/k_{\rm B}T}-1}\right) = 0\,, \tag{2.17}$$

in which, substituting the constant values we find that

$$\left(\frac{\nu_{\rm max}}{\rm GHz}\right) = 58.789\left(\frac{T}{\rm K}\right)\,. \tag{2.18}$$

The same analysis can be done in the wavelength λ space, resulting in

$$\left(\frac{\lambda_{\rm max}}{\rm cm}\right)\left(\frac{T}{\rm K}\right) = 0.28978\,. \tag{2.19}$$

Equations (2.18) and (2.19) are both known as Wien's displacement law. If (2.14) is far from the maximum, the distribution (2.12) can be approximated by simpler expressions.

Let us investigate the case where $h\nu \ll k_{\rm B}T$. This will lead us to the Rayleigh-Jeans law. An expansion of the exponential

$${\rm e}^{h\nu/k_{\rm B}T} \approx 1 + \frac{h\nu}{k_{\rm B}T} + \dots\,, \tag{2.20}$$

applied to (2.12) results in

$$B_{\mathrm{RJ}}(\nu, T) = \frac{2\nu^2}{c^2} k_{\mathrm{B}} T \,. \tag{2.21}$$

This is the classical limit of the Planck law since it does not contain Planck's constant. We can easily find the regime where this result is valid by inserting the numerical values for k_{B} and h into $h\nu \ll k_{\mathrm{B}}T$. This will give us that the Rayleigh-Jeans relation holds for frequencies

$$\frac{\nu}{\mathrm{GHz}} \ll 21 \left(\frac{T}{K}\right) . \tag{2.22}$$

This means that the Eq. (2.21) can be used for all thermal radio sources (with some exceptions). Eq. (2.21) can be used for studies of cosmic sources at centimeters and longer wavelengths. Since the BINGO radio window is inside this regime, this result is particularly relevant to the analysis of FRBs presented in this dissertation.

Now, note that we can compare Eq. (2.11) and (2.21) to get one of the main features of the Rayleigh-Jeans law: the fact that in this radio window, the brightness and the thermodynamic temperature of the black body that emits this radiation are strictly proportional,

$$I_\nu = \frac{2\nu^2}{c^2} k_{\mathrm{B}} T \,. \tag{2.23}$$

In radio astronomy, it is used to measure the brightness of an extended source by its brightness temperature T_{B}. This is the temperature that would result in the given brightness if inserted into the Rayleigh-Jeans law,

$$T_{\mathrm{B}} = \frac{c^2}{2k_{\mathrm{B}}\nu^2} I_\nu = \frac{\lambda^2}{2k_{\mathrm{B}}} I_\nu \,. \tag{2.24}$$

Putting Eq. (2.24) into (2.6), we have

$$S_\nu = \frac{2k_{\mathrm{B}}\nu^2}{c^2} T_{\mathrm{B}} \Delta\Omega \,, \tag{2.25}$$

In terms of the flux S_ν, the brightness temperature can be written as

$$T_\mathrm{B} = \frac{c^2}{2k_\mathrm{B}\nu^2}\frac{S_\nu}{\Delta\Omega}\,. \tag{2.26}$$

For very brief transient signals such as FRBs, we can approximate $\Delta\Omega$ by introducing the parameter cW where W is the burst or pulse width. This parameter expresses the size of the emitting region as the light travel time in a causally connected region. Furthermore, the area of the causally connected region is $\pi(cW)^2$, thus the solid angle $\Delta\Omega$ for a transient is

$$\Delta\Omega \approx \frac{\pi(cW)^2}{d_{\mathrm{L}^2}}, \tag{2.27}$$

where d_L is the angular diameter distance. So, the brightness temperature for a transient radio signal is

$$T_\mathrm{B} = \frac{1}{2\pi k_\mathrm{B}}\frac{S_\nu d_\mathrm{L}^2}{(\nu W)^2}\,, \tag{2.28}$$

which is equation 1.1, that creates a phase space for these signals.

2.1.4 The Nyquist theorem

The thermal motion of the electrons in the resistor will produce a current $i(t)$ which forms a random input to the amplifier. Though the mean value of this current will be zero, its RMS value will not. Since $\langle i^2\rangle \neq 0$ represents power, the resistor provides a power input to the amplifier. This is the Johnson noise, which was investigated by H. Nyquist in 1929 and can be compared to the random walk of a particle in Brownian motion with the addition of a friction term.

The average power per unit bandwidth produced by the resistor R in the circuit shown in Fig. 2.3 is

$$P_\nu = \langle iv\rangle = \frac{\langle v^2\rangle}{2R} = \frac{1}{4R}\langle v_\mathrm{N}^2\rangle\,, \tag{2.29}$$

where $v(t)$ is the voltage that is produced by i across R, and $\langle\ldots\rangle$ indicates a time average. The first factor $1/2$ arises from the need to transfer maximum power to the element on the right. This condition is met by setting $R_\mathrm{x} = R$; then $i = v/2R$. The

second factor 1/2 arises from the time average of v^2. An analysis of the random walk process now shows that

$$\langle v_{\mathrm{N}}^2 \rangle = 4Rk_{\mathrm{B}}T\,. \tag{2.30}$$

Inserting such expression into (2.29), we obtain

$$P_v = k_{\mathrm{B}}T\,. \tag{2.31}$$

Then, the available noise power of a resistor is proportional to its temperature, the noise temperature T_{N}, and independent of the value of R.

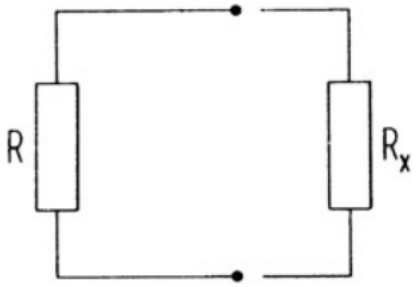

Figure 2.3: A sketch of a circuit containing a resistor R, to illustrate the origin of Johnson noise. The resistor R, on the left, at a temperature T, provides a power $k_{\mathrm{B}}T$ to a matched load R_{X}, on the right.

2.2 Descriptive Antenna Parameters

We shall now introduce some other basic concepts, but this time related to antenna parameters. In general, most antenna systems, especially those with high gain and directivity used in radio astronomy and communications must be analyzed using detailed numerical models such as GRASP since there is blockage by support structures. The following sections will present a simple description of antenna properties, which allows one to characterize the antenna properties based on astronomical measurements.

2.2.1 Power pattern

We introduce the concept of power pattern $P(\theta, \varphi)$ of an antenna. The power pattern refers to the directional (angular) dependence of the power of the radio waves from the antenna or other source. Often, one measures the normalized power pattern $P_n(\theta, \varphi)$, not the power pattern,

$$P_n(\theta, \varphi) = \frac{1}{P_{\max}} P(\theta, \varphi), \tag{2.32}$$

where $P_{\max}$ stands for the maximum value of $P(\theta, \varphi)$.

It is also useful to define the gain (or directive gain, or even directivity) $G(\theta, \varphi)$. Consider the power pattern of the antenna used as a transmitter. If the total spectral power, $\mathcal{P}_\nu$ in [W Hz^{-1}] is fed into a lossless isotropic antenna, this would transmit P power units per solid angle per Hertz. Then the total radiated power at frequency ν is $4\pi P_\nu$. In a realistic, but still, lossless antenna, a Power $P(\theta, \varphi)$ per unit solid angle is radiated in the direction (θ, φ). We, then, define the gain $G(\theta, \varphi)$ as the

$$P(\theta, \varphi) = G(\theta, \varphi) P\,, \tag{2.33}$$

or

$$G(\theta, \varphi) = \frac{4\pi P(\theta, \varphi)}{\iint P(\theta, \varphi)\, \mathrm{d}\Omega}. \tag{2.34}$$

Thus, the gain is also a normalized power pattern to (2.32), but with the difference that the normalizing factor is $\iint P(\theta, \varphi)\, \mathrm{d}\Omega / 4\pi$. This is the gain relative to a lossless isotropic source.

2.2.2 Main beam solid angle

The beam solid angle Ω_A of an antenna is given by

$$\Omega_\mathrm{A} = \iint\limits_{4\pi} P_\mathrm{n}(\theta, \varphi)\, \mathrm{d}\Omega = \int\limits_0^{2\pi} \int\limits_0^{\pi} P_\mathrm{n}(\theta, \varphi) \sin\theta\, \mathrm{d}\theta\, \mathrm{d}\varphi\,, \tag{2.35}$$

which is measured in steradians (sr). The integration is performed over the entire surface of a sphere, such that Ω_A represents the solid angle of an ideal antenna with $P_n = 1$ across Ω_A and $P_n = 0$ elsewhere. However, such an antenna does not exist in reality. Most antennas have a normalized power pattern that is much larger within a certain range of angles than for the rest of the sphere. This range is known as the antenna's main beam or main lobe, while the other parts are called side lobes or back lobes (see Fig. 2.4). These properties are well-defined for actual situations up to the shortest operating wavelengths. However, much of the power may enter through side lobes at the shortest wavelength, even though there is still a main beam. Moreover, the efficiency of the main beam may vary significantly depending on the elevation. Therefore, accurately calibrating a radio telescope at the shortest wavelengths can be challenging. In analogy to (2.35) we define the main beam solid angle Ω_{MB} by

$$\Omega_{\mathrm{MB}} = \iint\limits_{\text{main lobe}} P_{\mathrm{n}}(\theta, \varphi)\, \mathrm{d}\Omega\,. \tag{2.36}$$

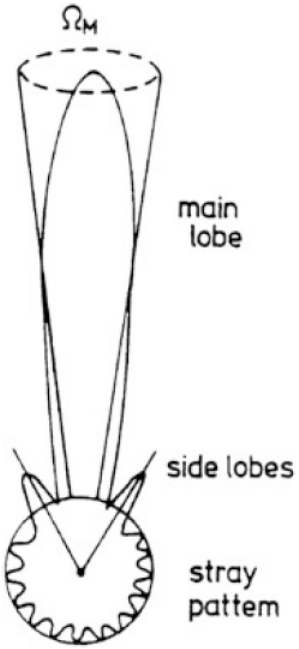

Figure 2.4: A polar power pattern showing the main beam, and near and far side lobes. The weaker far side lobes have been combined to form the "stray pattern".

The effectiveness of an antenna as a device for measuring direction depends on how much of the power pattern is concentrated in the main beam. If a significant portion of the received power comes from the side lobes instead, measurements can be difficult to perform. It is appropriate to define a main beam efficiency or (usually) beam efficiency, η_{B}, by

$$\eta_{\mathrm{B}} = \frac{\Omega_{\mathrm{MB}}}{\Omega_{\mathrm{A}}} \,. \tag{2.37}$$

The angular size of the main beam has no bearing on the main beam efficiency. In fact, a small antenna with a broad main beam can have a high beam efficiency. The beam efficiency η_{B} represents the proportion of power concentrated in the main beam and can be adjusted. This can be achieved simply by choosing appropriate primary feeds and foci. When the full width at half power (FWHP) beam width is well-defined, the position of an isolated source can be accurately determined by dividing the FWHP by the signal-to-noise (S/N) ratio. Therefore, it is possible to determine positions with precision to a small fraction of the FWHP beam width.

Substituting (2.35) into (2.34) where $P_{\mathrm{n}} = 1$ it is easy to see that the maximum directive gain G_{max} or directivity $\mathcal{D}$ can be expressed as

$$\mathcal{D} = G_{\mathrm{max}} = \frac{4\pi}{\Omega_{\mathrm{A}}} \,. \tag{2.38}$$

The half-power beam width (HPBW) is typically used to describe the angular range of the main beam, which refers to the angle between the points on the main beam where the normalized power pattern drops to half of its maximum value. This measurement is also known as the full-width to half-power (FWHP). Although less common, other measures include the beam width between the first nulls (BWFN) or the equivalent width of the main beam (EWMB), which is defined as follows:

$$\mathrm{EWMB} = \sqrt{\frac{12}{\pi}\,\Omega_{\mathrm{MB}}} \,. \tag{2.39}$$

When dealing with elliptical main beams, it is necessary to determine the widths in both orthogonal directions. The beam width is influenced by the antenna's geometric size and the wavelength utilized, and the specific beam size is dependent on the grading functions and illumination.

2.2.3 Effective aperture

Assume an antenna intercepts a plane wave with power density $|\langle \mathbf{S} \rangle|$. The antenna extracts a specific amount of power P_e from this wave. We will then call the fraction

$$A_\mathrm{eff} = \frac{P_\mathrm{e}}{|\langle \mathbf{S} \rangle|} \tag{2.40}$$

as the effective aperture of the antenna A_eff. Such quantity can be likened to a cross-section in particle physics, with units of m^2. By comparing this to the geometric aperture A_g, we can establish the aperture efficiency η_A using the formula

$$A_\mathrm{eff} = \eta_\mathrm{A} A_\mathrm{g} \,. \tag{2.41}$$

For a calculation of the effective aperture, the peak value of A_e is used; this is the direction of the telescope axis. The directivity is related to A_e by

$$\mathcal{D} = G_\mathrm{max} = \frac{4\pi A_\mathrm{eff}}{\lambda^2} \,, \tag{2.42}$$

which according to (2.38) is equivalent to

$$A_\mathrm{eff}\, \Omega_\mathrm{A} = \lambda^2 \,. \tag{2.43}$$

Eq. 2.43 is known as the antenna theorem.

2.2.4 Antenna temperature

If a normalized power pattern $P_{\mathrm{n}}(\theta, \varphi)$ is directed towards a brightness distribution $B_\nu(\theta, \varphi)$ in the sky using a receiving antenna, then the output terminals of the antenna will have a total power per unit bandwidth, $\mathcal{P}_\nu$ given by

$$\mathcal{P}_\nu = \frac{1}{2}\, A_{\mathrm{eff}} \iint B_\nu(\theta, \varphi)\; P_{\mathrm{n}}(\theta, \varphi)\; \mathrm{d}\Omega = \frac{1}{2} A_{\mathrm{eff}}\, S_\nu\,. \tag{2.44}$$

In the Rayleigh-Jeans limit, the brightness distribution can be replaced by an equivalent distribution of brightness temperature, as per the definition. By applying the Nyquist theorem (2.31), we can introduce an equivalent antenna temperature, denoted as T_{A} by

$$\mathcal{P}_\nu = k_{\mathrm{B}} T_{\mathrm{A}}\,, \tag{2.45}$$

or

$$T_{\mathrm{A}} = \frac{1}{2k_{\mathrm{B}}}\, A_{\mathrm{eff}} \iint B_\nu(\theta, \varphi)\; P_{\mathrm{n}}(\theta, \varphi)\; \mathrm{d}\Omega = \frac{1}{2k_{\mathrm{B}}}\; A_{\mathrm{eff}}\, S_\nu\,. \tag{2.46}$$

The definition of antenna temperature establishes a connection between the antenna's output and the power from a matched resistor. The temperature of the resistor is considered as the antenna temperature when the power levels of both are identical. Instead of the effective aperture A_{eff} we can introduce the beam solid angle Ω_{A} using (2.43). In this case, (2.44) becomes

$$T_{\mathrm{A}}(\theta_0, \varphi_0) = \frac{\int T_{\mathrm{B}}(\theta, \varphi) P_{\mathrm{n}}(\theta - \theta_0, \varphi - \varphi_0) \sin\theta\; \mathrm{d}\theta\; \mathrm{d}\varphi}{\int P_{\mathrm{n}}(\theta, \varphi)\, \mathrm{d}\Omega}\,, \tag{2.47}$$

which is the convolution of the brightness temperature with the beam pattern of the telescope. The brightness temperature T_{B} is equivalent to the thermodynamic temperature of the radiating material, but only when it pertains to thermal radiation in the Rayleigh-Jeans limit originating from an optically thick source. In all other instances, T_{B} is merely a useful parameter that is generally dependent on frequency. It is possible to reconstruct the layout of extended sources, all the way down to the beam

size. This process is comparable to the "Inverse Problem" in various fields, including image processing. To obtain the desired quantity T_{B}, equation (2.47) must be inverted, as T_{A} is the quantity that is actually measured. This equation is a first-kind integral equation that, in theory, can be solved if the full range of T_{A} and P_{n} is known. However, in practice, the inversion can only be performed approximately, as both T_{A} and P_{n} are typically only known for a limited range of values, and the measured data is not error-free. Therefore, only an approximate deconvolution is usually carried out. A special case arises when the source distribution $T_{\mathrm{B}}(\theta, \varphi)$ has a small extent relative to the telescope beam, which is known as a "point source". In such cases, the best estimate for the upper limit of the actual full width at half maximum (FWHM) source size is half the FWHM of the telescope beam. The challenge is that even minor errors in either the beam shape or the measurement can result in significant errors in the resulting source distribution.

2.3 The Radiometer Equation

To work properly, a receiver must be able to detect weak signals even in the presence of noise, which requires a high degree of sensitivity. However, every measuring device has its limits when it comes to sensitivity due to the influence of noise on both the receiver input and the device itself. This limit can be expressed as a function of receiver parameters. Even when no external input is connected to a receiver, there will still be an output signal due to thermal noise generated by the device, which is then amplified along with the signal. Since both the signal and noise share similar statistical characteristics, they cannot be differentiated from one another. Before going further on this topic, I will briefly explain how a receiving system works to establish the jargon that I will be using.

2.3.1 Receiving systems

Fig. 2.5 shows a super-heterodyne receiving system very similar to what is used in most radio telescopes today. Its main components are:

- A low noise amplifier (LNA) and filter. When dealing with frequencies higher than approximately 300 MHz, it is common practice to cool the LNA cryogenically to a temperature of around 15 K.
- A mixer is utilized to convert ν_{RF}, which represents the central frequency of the desired frequency band $\Delta\nu_{\mathrm{RF}}$, to an intermediate frequency ν_{IF} that is more convenient for all receiving systems on the telescope. The local oscillation signal is typically phase-locked to the observatory's master oscillator, which is commonly a hydrogen maser frequency standard. RF and IF stand for received frequency and intermediate frequency respectively.
- An intermediate frequency amplifier and filter which limits the bandwidth to $\Delta\nu_{\mathrm{IF}}$.
- A square law detector (i.e. its output voltage is proportional to the input power) followed by an integrator which averages the detector output for $\Delta\tau$ seconds.

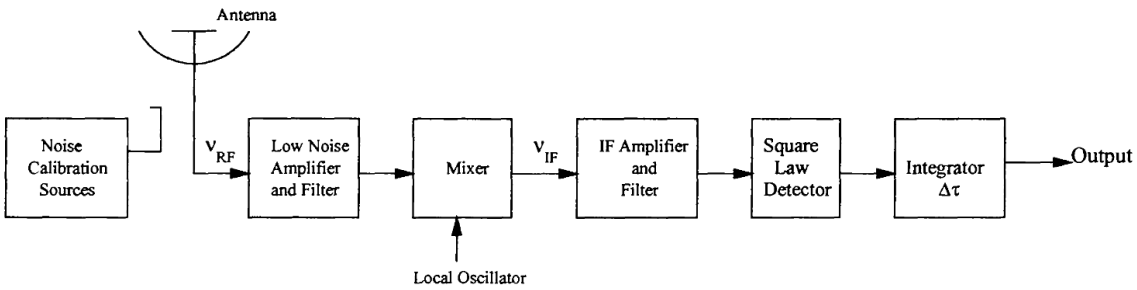

Figure 2.5: A schematic diagram of a super-heterodyne receiving system.

In this receiving system, the ability to detect minor variations in power at the output terminals of our telescope caused by a radio source with antenna temperature T_{A} is determined by several factors. These factors include the level of additive noise

power, typically represented as a temperature, known as the system noise temperature $T_{\rm sys}$, the pre-detection bandwidth $\Delta\nu_{\rm IF}$, and the post-detection integration time $\Delta\tau$. Since the noise contributions from sources such as atmosphere, ground, and receiver ($T_{\rm i}$) are additive, $T_{\rm sys}$ can be written as

$$T_{\rm sys} = \sum T_{\rm i}\,. \tag{2.48}$$

Now, we shall return to the question of how we detect the presence of the power due to a radio source as represented by $T_{\rm A}$, in the presence of the additive noise power represented by $T_{\rm sys}$?

2.3.2 Minimum detectable flux

After passing through the integrator (refer to Fig. 2.6), the voltage at the output is directly proportional to the sum of the input power from the source and the additive noise, which are in turn proportional to $T_{\rm A}$ and $T_{\rm sys}$, respectively. In order for this to hold, it is necessary that the input voltage resulting from $T_{\rm A}$ and $T_{\rm sys}$ is uncorrelated, what is consistently true. Consequently, the expected value of the integrator's output voltage attributed to the source is given by

$$\langle v_{\rm A}(t)\rangle = G\,T_{\rm A}\,, \tag{2.49}$$

where G stands for the total gain between the input signal and the output of the receiver and $\langle\ \rangle$ denotes the time-averaged value of the output. Moreover, the expected value due to the mean noise power is

$$\langle v_{\rm n}(t)\rangle = G\,T_{\rm sys}\,, \tag{2.50}$$

where the gain for (2.49) and (2.50) are the same since both signals are passing through the same circuit components inside the receiver.

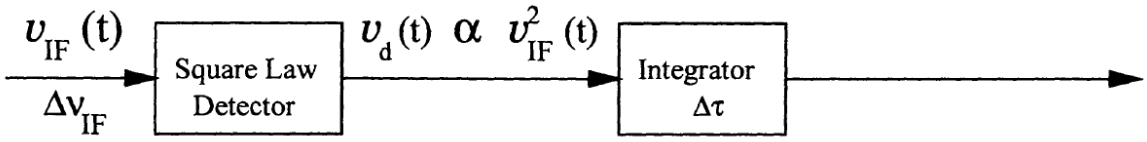

Figure 2.6: A schematic diagram showing the last two stages of the receiver system.

The signal-to-noise ratio (SNR) at the output of the receiver is given by

$$\mathrm{SNR} = \frac{\langle v_\mathrm{A}(t)\rangle}{\langle v_\mathrm{n}(t)\rangle} = \frac{G\,T_\mathrm{A}}{G\,T_\mathrm{sys}} = \frac{T_\mathrm{A}}{T_\mathrm{sys}}\,. \tag{2.51}$$

The SNR is a measure that compares the level of a desired signal to the level of noise. It is a way to express how much a signal can be distinguished from noise in a particular system or application. A high SNR indicates that the signal is stronger than the noise, making it easier to detect and interpret. A low SNR, on the other hand, indicates that the noise level is high compared to the signal, what can lead to errors or loss of information in the communication system. Therefore, a higher SNR is generally desired in most communication applications, as it can improve the quality and reliability of the transmitted signal, the same in radio astronomy.

The determining factor for our ability to detect the average power source $\langle v_\mathrm{A}(t)\rangle$ in the presence of $\langle v_\mathrm{n}(t)\rangle$ is not the mean value of $\langle v_\mathrm{n}(t)\rangle$, but rather its level of fluctuation measured by its root mean square (RMS) or standard deviation. The desired quantity is

$$\sigma_\mathrm{n} = [\langle v_\mathrm{n}^2(t)\rangle - \langle v_\mathrm{n}(t)\rangle^2]^{1/2}\,. \tag{2.52}$$

I will be using an intuitive method to derive σ_n. A rigorous derivation can be found in Rohlfs & Wilson (2013). The integrator operates as an averaging device, combining n independent estimates of the output voltage from the square law detector to compute the mean value. The standard deviation of this mean, denoted as σ_n, can be expressed as $\sigma/\sqrt{n}$ (e.g. Papoulis & Unnikrishna Pillai, 2002), where σ represents the standard deviation of the output voltage from the square law detector. To determine σ_n accurately, the values of n and σ must be known.

When the input to the square law detector is a noise-like voltage following Gaussian statistics, the standard deviation of the output voltage, $v_{\rm d}(t)$, from the square law detector is equal to its mean value. This relationship is described, for example, in Ulaby et al. (1981). Hence, we have that,

$$\sigma = \langle v_{\rm d}(t) \rangle = G\, T_{\rm sys}\,. \tag{2.53}$$

What is n? A signal with a bandwidth $\Delta\nu$ can fluctuate on a time scale, Δt, given by

$$\Delta\nu\Delta t = 1\,. \tag{2.54}$$

Voltage samples separated by time Δt can be regarded as independent. Therefore, the number of independent samples, n, averaged by the integrator is

$$n = \frac{\Delta\tau}{\Delta t} = \Delta\tau\Delta\nu_{\rm IF}\,. \tag{2.55}$$

The signal-to-r.m.s. noise ratio (**the Radiometer Equation**; henceforward simply signal-to-noise ratio) $\mathrm{SNR_{RMS}}$ can now be written as:

$$\mathrm{SNR_{RMS}} = \frac{\langle v_{\rm A}(t) \rangle}{\sigma_{\rm n}} = \frac{\langle v_{\rm A}(t) \rangle}{\sigma}\sqrt{n} = \frac{T_{\rm A}}{T_{\rm sys}}\sqrt{\Delta\tau\Delta\nu_{\rm IF}}\,. \tag{2.56}$$

For unity $\mathrm{SNR_{RMS}}$, the equivalent fluctuation in the antenna temperature is given by

$$\Delta T_{\rm A} = \frac{T_{\rm sys}}{\sqrt{\Delta\tau\Delta\nu_{\rm IF}}}\,. \tag{2.57}$$

Equations (2.56) and (2.57) represent the fundamental relation between system noise, bandwidth, integration time, and RMS fluctuations: for a given system, the improvement in the RMS noise cannot be better than given in Eq. (2.57). Systematic errors will only increase $\Delta T_{\rm A}$, although the time behavior may follow relation (2.57). To emphasize, I repeat that $\Delta T_{\rm sys}$ is the noise from the entire system. That is, it includes the noise from the receiver, atmosphere, ground, and source. Therefore $\Delta T_{\rm A}$

will be larger for an intense source.

By inserting equation (2.46) into (2.57) we can substitute the antenna temperature by the source flux to find the minimum detectable flux in a given frequency $S_{\nu,\min}$ by a telescope's receiver. We have then,

$$S_{\nu,\min} = \frac{2k_{\mathrm{B}}T_{\mathrm{sys}}}{A_{\mathrm{eff}}\sqrt{\Delta\tau\Delta\nu_{\mathrm{IF}}}}\,, \tag{2.58}$$

known as sensitivity. Since the sensitivity is better in the maximum of the telescope power pattern, we also may define the forward gain as

$$G = \frac{A_{\mathrm{eff}}}{2k_{\mathrm{B}}}\,, \tag{2.59}$$

which represents the ratio of the signal transmitted in the maximum direction to the signal in reference or standard antenna direction.

Equations (2.56), (2.57) (2.58) still need two corrections. The first is for the number of independent samples n. If the receiver is detecting more than one polarization, n is going to be multiplied by the number of polarizations n_{p}. The second is the noise performance K which depends on the receiver type. Hence, these three relations can be written as

$$\mathrm{SNR}_{\mathrm{RMS}} = \frac{T_{\mathrm{A}}\sqrt{n_{\mathrm{p}}\Delta\tau\Delta\nu_{\mathrm{IF}}}}{KT_{\mathrm{sys}}}\,, \tag{2.60}$$

$$\Delta T_{\mathrm{A}} = \frac{KT_{\mathrm{sys}}}{\sqrt{n_{\mathrm{p}}\Delta\tau\Delta\nu_{\mathrm{IF}}}}\,, \tag{2.61}$$

and

$$S_{\nu,\min} = \frac{KT_{\mathrm{sys}}}{G\sqrt{n_{\mathrm{p}}\Delta\tau\Delta\nu_{\mathrm{IF}}}}\,. \tag{2.62}$$

With these relations, I conclude this chapter. I have presented all the necessary background in radio astronomy to push forward in the discussion of this thesis. We now shall discuss BINGO and the BINGO Interferometry System.

Chapter 3

The BINGO Interferometry System

In this chapter, I will be covering some of BINGO's technical details that will be relevant to the scope of assumptions made at the length of this thesis. Further details of the telescope can be found in the BINGO's series of papers (I to VII respectively): Abdalla et al. (2022a), Wuensche et al. (2022), Abdalla et al. (2022b), Liccardo et al. (2022), Fornazier et al. (2022), Zhang et al. (2022) and Costa et al. (2022). After this brief exposure, I will present the BINGO Interferometry System (BIS), and its setups to search for FRBs followed by how we are simulating the telescope's performance.

3.1 Baryon Acoustic Oscillations from Integrated Neutral Gas Observations

The BINGO project[1], which stands for **B**aryon Acoustic Oscillations (BAO) from **I**ntegrated **N**eutral **G**as **O**bservations, is a radio telescope project centered around a single dish telescope. Its primary objective is to observe the 21-cm line, which is the hyperfine interaction of atomic hydrogen. The project will cover a sky area of 6000 square degrees within a redshift range of 0.127 to 0.449 (corresponding to a frequency

[1]BINGO is funded by several Brazilian and Chinese agencies. From the Brazilian side, the major supporters are FAPESP and the Government of Paraíba. China is the main partner, both in terms of funding as well as in terms of scientific personnel. Brazilian and Chinese companies are working for the BINGO construction, mainly Alltec and IBRTEL from Brazilian side, and CETC54 from the Chinese counterpart.

span of 980 to 1260 MHz) with an angular resolution of around 40 arcmin. In phase 1, the project will have 28 feed horns and receivers with dual polarization and is designed to achieve a system temperature of about 70 K. Final numbers will depend on financial and technical achievements. For phase 2, the project aims to increase the number of feed horns up to 56 and update the receivers to achieve a smaller system temperature.

Given its abundance, hydrogen is considered to be a representative element for mapping (through the neutral hydrogen radiation) the overall matter content in the Universe, without any bias. Using the technique of Intensity Mapping (IM; Madau et al. 1997; Bharadwaj & Sethi 2001), BINGO will provide detailed maps of the matter distribution in its redshift range, enabling the extraction of BAO measurements that can be compared to those obtained through optical observations Eisenstein et al. (2005). Additionally, owing to the telescope's characteristics, BINGO can study phenomena at very short timescales, making it an intriguing tool for researching pulsars and the primary focus of this thesis: **FRBs**. Fig. 3.1 shows a full-sky map for extragalactic H_I indicating BINGO's survey area from declination approximately $-22.5^o < \delta < -10.0^o$.

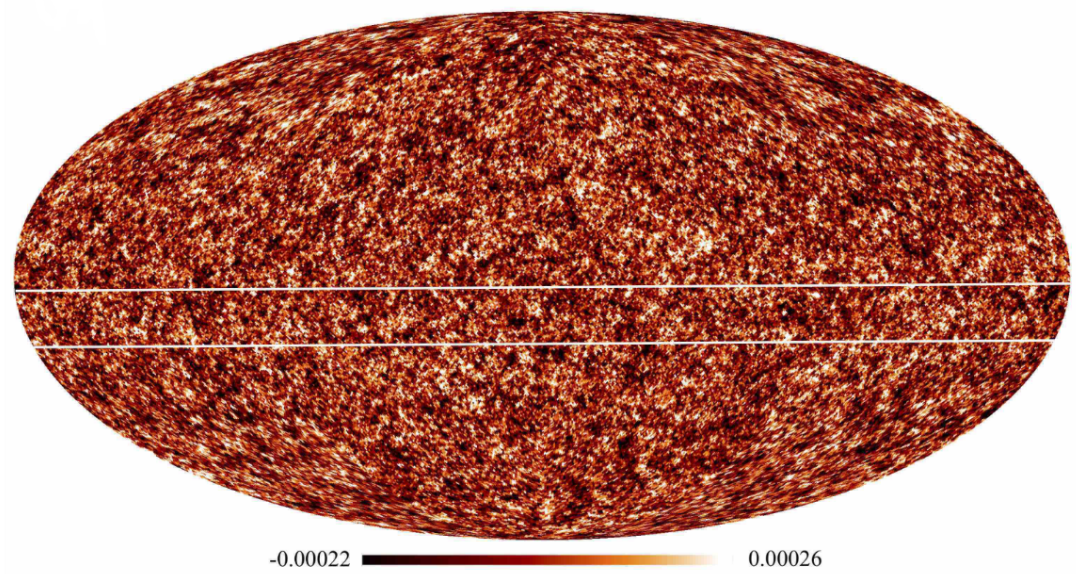

Figure 3.1: Full-sky maps of the cosmological signal of extragalactic H_I for a frequency slice $\nu \approx 1.1$ GHz. The stripe defined by the white solid lines is the sky region covered by BINGO. Temperature is given in K. Equatorial coordinates. Credits: Liccardo et al. (2022).

The BINGO telescope is currently under construction in a remote location in Aguiar, Paraíba, northeastern Brazil (latitude: 7°2′29″ S, longitude: 38°16′5″ W; Fig. 3.2). The site is situated amidst hills, has a very small population nearby, and hardly any mobile signal coverage in the surrounding areas. To maintain radio silence, the project has requested a "radio-quiet" zone from the local authorities and ANATEL, the Brazilian regulator agency for telecommunications. The process of selecting the site and measuring Radio Frequency Interference (RFI) is described in Peel et al. (2019), and an artist's view of the telescope can be seen in Fig. 3.3. I will now give a brief description of the optical design of the telescope.

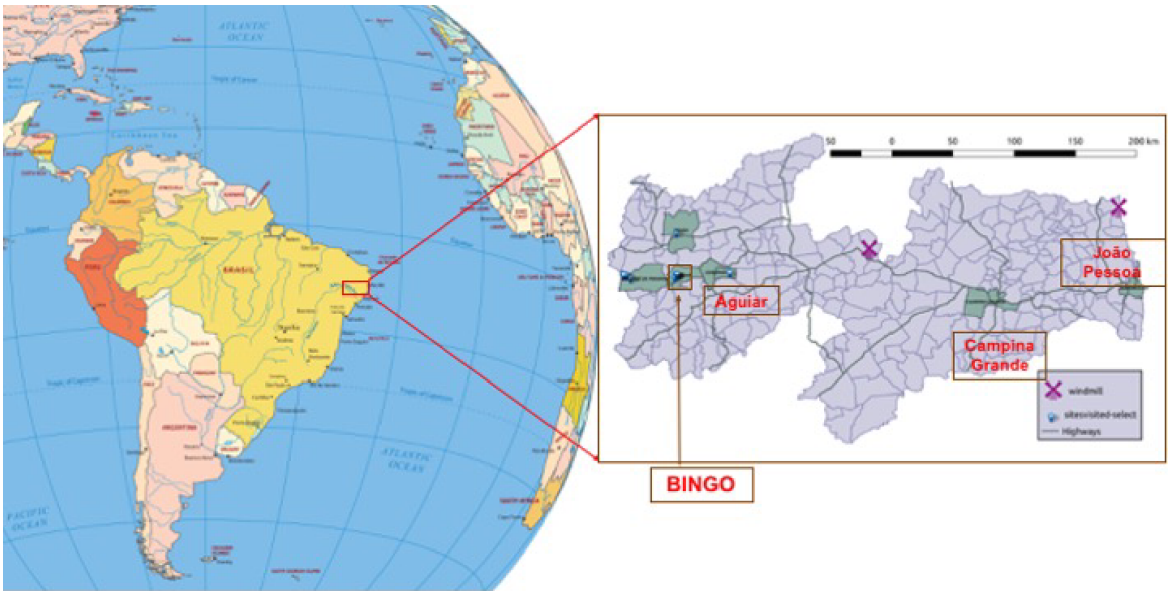

Figure 3.2: Map of BINGO location. Left: Paraíba state, marked by the red rectangle, is on the northeastern Brazilian coast. Brazil area, in yellow, is depicted on the map of South America. Right: Paraíba state map, with county subdivisions, with João Pessoa (the capital), Campina Grande (the headquarters of Universidade Federal de Campina Grande), and Aguiar counties highlighted.

Figure 3.3: Artist's view of the telescope.

3.1.1 Optics

The optical system is designed based on the off-axis, crossed-Dragone configuration (Dragone 1978). It consists of a primary offset paraboloid reflector with a semi-major axis of 25.5 m and a secondary offset hyperboloid reflector with a semi-major axis of 18.3 m. The primary reflector has a total area of 1602 m^2 and an effective area of approximately 1120 m^2. The telescope has a focal length of 63.2 m and points to a declination of $\delta = -15^o$. The secondary reflector is illuminated by the focal plane array, providing an instantaneous field-of-view of 88 square degrees with an angular resolution (FWHM; full width at half maximum) of approximately 0.67^o.

Figs. 3.4, 3.5 and 3.6 provide a summary of the optical design and engineering efforts for the entire telescope, along with its placement on the site. Additionally, Fig. 3.6 illustrates the topographical features of the area, highlighting how the hill on the western side of the terrain serves as a barrier, effectively minimizing radio frequency interference (RFI) contamination.

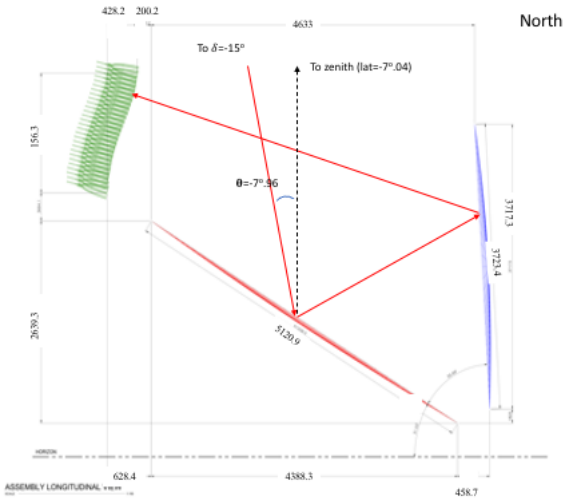

Figure 3.4: BINGO optics schematics: the primary mirror is in the center, facing north pointing to $\delta = -15^o$. All dimensions are in millimeters.

The final design ensures minimal optical aberration and beam ellipticity, even for beams located at the outer edge of the focal plane. The horn distribution across the focal plane ensures that each horn independently observes a distinct patch of the sky

in terms of declination, as indicated by the distances presented in Fig. 3.7. This horn distribution corresponds to the optimal configuration of the beam pattern, as displayed in Fig. 3.8, and represents the most favorable arrangement of horns in terms of the uniformity of sky coverage. Please note the inverted positioning of the figures in relation to one another, which is due to the method used to map the sky. A schematic view of a horn in the hexagon cage can be seen in Fig. 3.9.

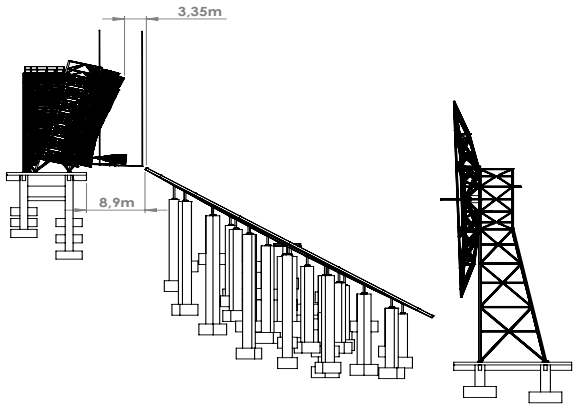

Figure 3.5: Engineering design based upon the dimensions and angles shown in Fig. 3.4. We note that the exact positions for the support structure foundations have already been calculated

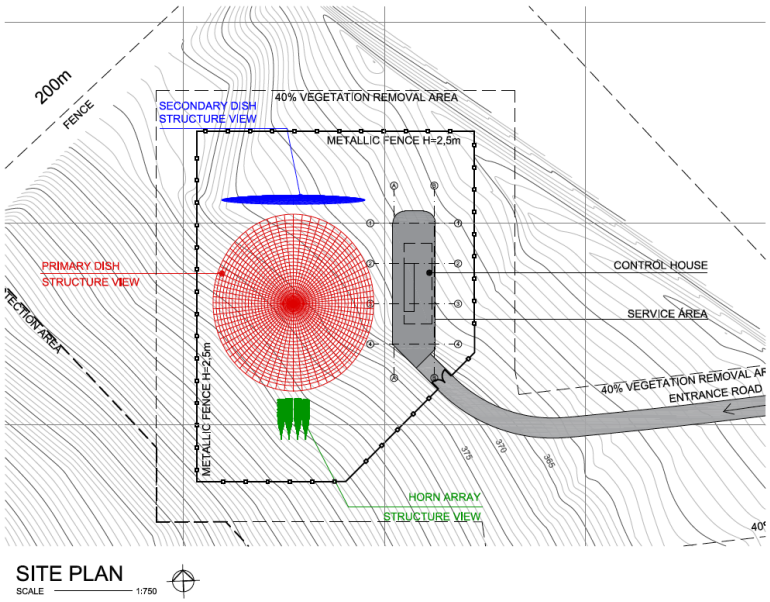

Figure 3.6: Plan view of the site, with the structure in Fig. 3.5 highlighted in blue, red, and green. The top of the figure points to the north. The control cabin is located on the southwestern part of the terrain, behind a hill and off the main view of the telescope.

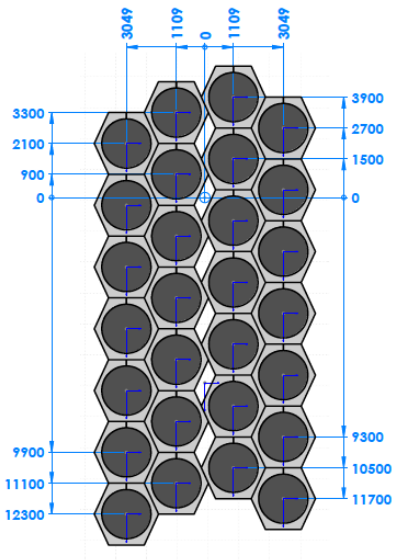

Figure 3.7: Horn arrangement in the focal plane for BINGO Phase 1. All dimensions are in millimeters

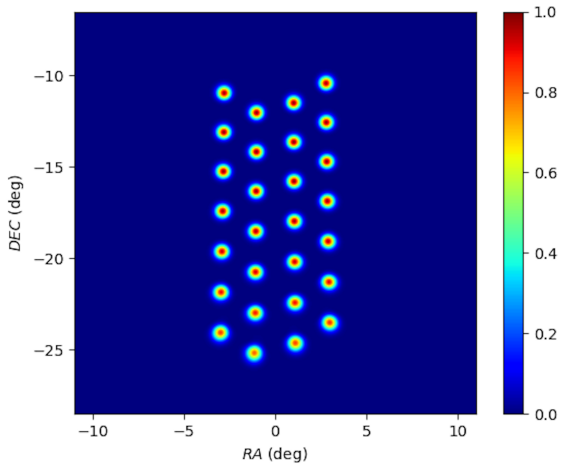

Figure 3.8: Beam pattern response in the focal plane, as looking at the sky in equatorial coordinates. The color scale on the right is the total intensity normalized to the peak amplitude.

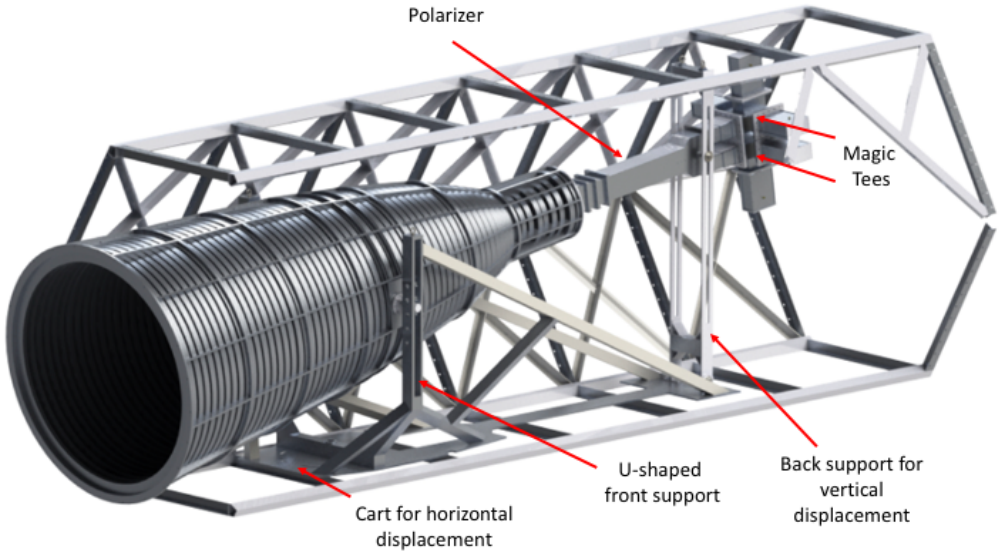

Figure 3.9: Hexagonal cage for the horn with dimensions 6500 mm(length) × 2400 mm(height) × 2600 mm(width). The horn is attached to a U-shaped support by the ring crossing its center of mass, for pivoting and vertical displacement, and to another structure connected to the end of the polarizer, on the opposite side of the horn mouth. The U-shaped support and the back structure are mounted on top of a cart that allows for longitudinal positioning of the horn.

3.2 The BINGO Interferometry System

The task of determining the redshift of the host galaxy is still a hard one. Indeed, to determine the distance one should localize the events with arcsecond precision. We can use other surveys to find their optical counterpart (Tendulkar et al. 2017; Bhandari et al. 2022). Localizing an FRB event is very important to understand the origin and environment of its progenitor, as well as to use its redshift determination to attack a few open problems in cosmology. The precise localization of the events is possible using interferometric techniques, where the data from different antennas are cross-correlated, pinpointing the origin of the emission. We want to correlate the data from a main telescope with data from its outriggers, which, in this context, are auxiliary smaller radio telescopes. Fig. 3.10 shows a BINGO outrigger (named BINGO Uirapuru) already installed in Campina Grande aiming for BINGO tests.

Figure 3.10: The BINGO Uirapuru is a radio telescope mounted with a prototype of the BINGO radio telescope's horn antenna. It is hosted at the Metrology Laboratory of the Electrical Engineering Department at the Federal University of Campina Grande at coordinates 7°12′41.9″S 35°54′29.5″W.

To improve BINGO's capability to detect and localize FRBs, outrigger units are being planned and designed. The instrumental requirements and capabilities of these outriggers are being determined using a combination of mock FRB catalogs, simulations of events, and detection forecasting. Aiming for the best performance to localize FRBs, a second kind of outrigger is also being considered. By coupling a mirror to the outrigger we can increase its directivity thus increasing the FRBs localization rate. Fig 3.11 shows a schematic with the mechanism. Hereafter I will refer to the outrigger without a mirror as a "naked horn".

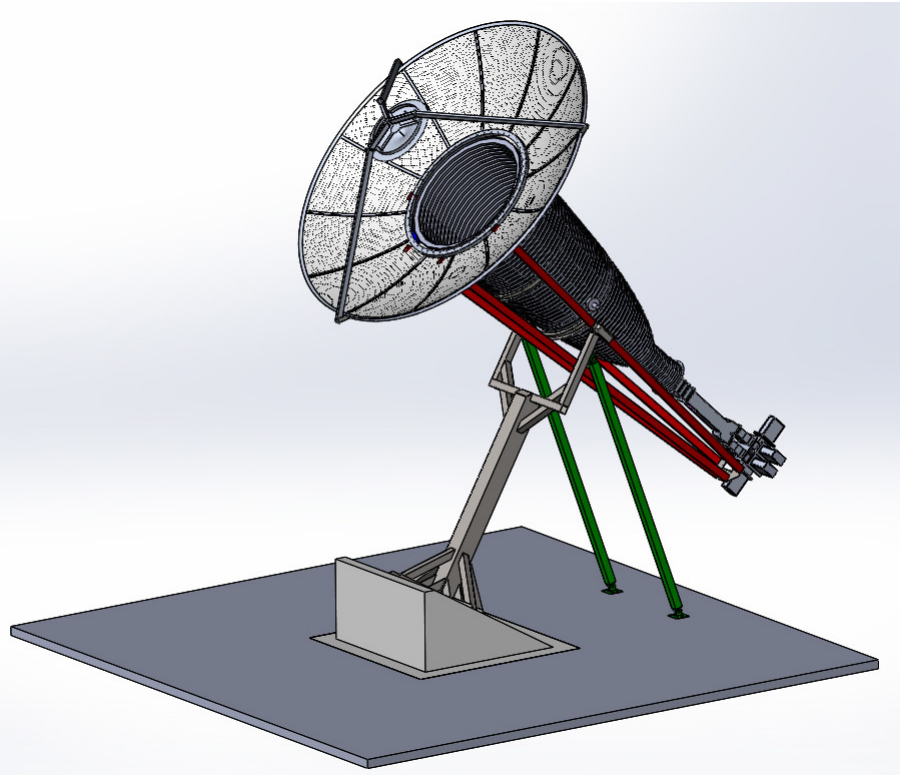

Figure 3.11: Scheme showing how the mirror is fixed in the outrigger to increase its directivity.

For the outriggers we choose four different types: the first one is simply a BINGO naked horn, and the other three consist of a horn with different mirror diameters (4 m, 5 m, 6 m). Besides being in different locations on Earth to perform interferometry, the outriggers should point to equivalent positions in the sky compared to the main telescope focal plane seen in Fig. 3.8. In this analysis, I will consider a perfect time delay, so the distance between the telescopes can be neglected (more on this in §3.2.1).

Each type of outrigger is pointed to the sky in four different ways, shown in Fig. 3.12, in a total of sixteen configurations (each setup for each mirror size and the naked horn).

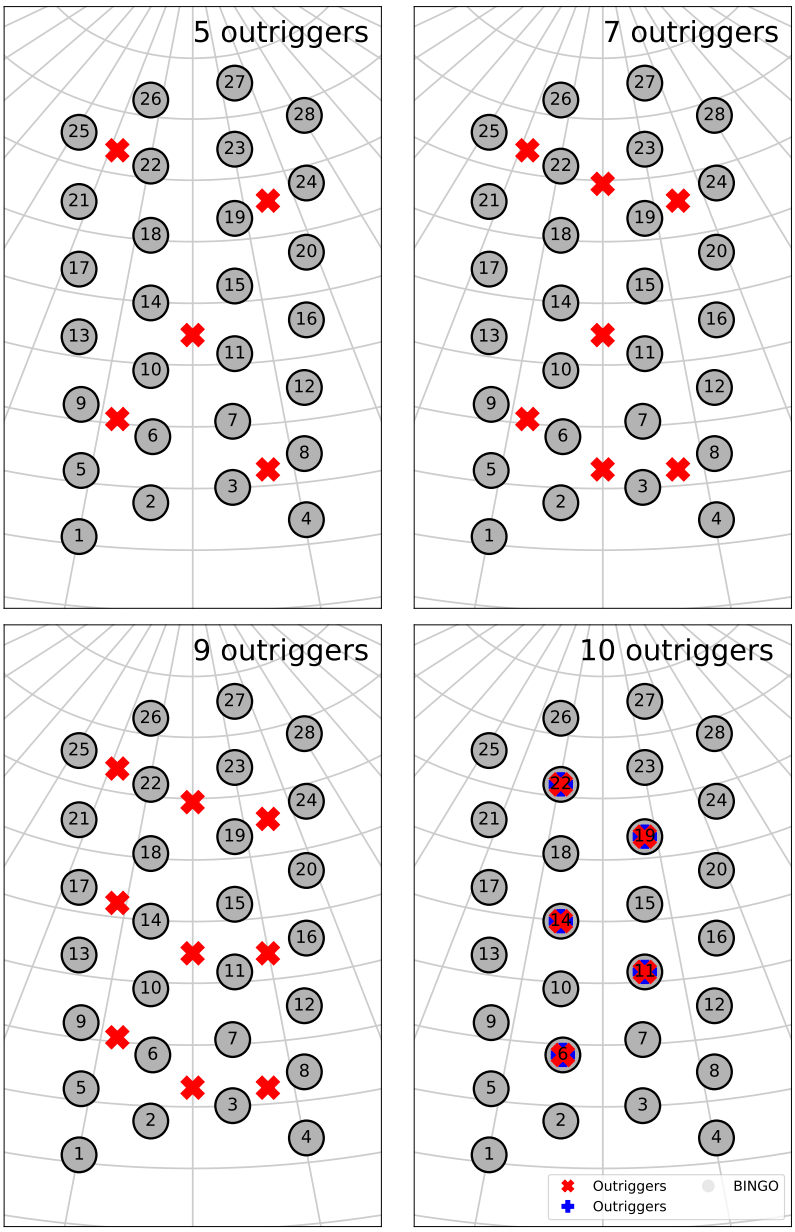

Figure 3.12: BINGO beams on the sky and outriggers, and four different outriggers pointing. Note that for the 10 outriggers, we have 2 outriggers pointing in exact same direction as a BINGO horn.

In this analysis, we suppose that radio telescopes are well characterized by only seven quantities: system temperature ($T_{\rm sys}$), forward gain (G), sensitivity constant (K, depends on the receiver type), number of polarizations (n_p), the frequency bandwidth

($\Delta\nu = \nu_2 - \nu_1$), a reference frequency ($\nu_1 < \nu_{\rm ref} < \nu_2$), and sampling time ($\tau$). An important derived quantity is the instrument noise

$$S_{\rm min}^{(0)} = \frac{K\, T_{\rm sys}}{G\sqrt{n_p \Delta\nu\, \tau}}\,, \tag{3.1}$$

known as sensitivity, which roughly defines the minimum detectable flux density assessed by a given instrument (Kraus et al. 1986). In BINGO's paper I, (Abdalla et al. 2022a) we assumed the telescope beam as being a top hat function, constant inside a given radius. Now, we assume a (more realistic) Gaussian beam pattern,

$$P_n(\mathbf{n}) = \exp\left(-4(\log 2)\frac{\theta^2}{\theta_{1/2}^2}\right)\,, \tag{3.2}$$

where θ is the angular separation to the beam center. Here, $\theta_{1/2}$ is the FWHM, related to G, and $\lambda_{\rm ref}$ ($c/\nu_{\rm ref}$) by

$$\theta_{1/2} \approx \sqrt{\frac{4\log 2}{\pi k_B G}}\lambda_{\rm ref}\,. \tag{3.3}$$

The forward gain G is related to the effective area ($A_{\rm eff}$) as

$$G = \frac{A_{\rm eff}}{2k_B}\,. \tag{3.4}$$

In this case, the signal of a point source, such as FRBs, will be contaminated by instrument noise which depends on its sky position ($\mathbf{n}$) as

$$S_{\rm min}(\mathbf{n}) = \frac{S_{\rm min}^{(0)}}{P_n(\mathbf{n})}\,, \tag{3.5}$$

which we name directional sensitivity. The normalized antenna pattern appears in the denominator as a matter of convenience, because it will appear in the numerator of Eq. (3.9).

The values of G, $S_{\rm min}^{(0)}$, and $\theta_{1/2}$ for the 28 independent BINGO beams are shown in Table 3.1 and for the outriggers in Table 3.2. For all telescopes we choose: $T_{\rm sys} = 70$ K, $\Delta\nu = \nu_2 - \nu_1 = 280$ MHz, $K = \sqrt{2}$ and $n_p = 2$.

Horn	$A_{\rm eff}$ (m^2)	G (mK/Jy)	$S^{(0)}_{\rm min}$ (mJy)	$\theta_{1/2}$ (arcmin)	Horn	$A_{\rm eff}$ (m^2)	G (mK/Jy)	$S^{(0)}_{\rm min}$ (mJy)	$\theta_{1/2}$ (arcmin)
1	637.8	231.0	572.7	49.3	15	634.1	229.6	576.0	49.4
2	646.3	234.0	565.2	49.0	16	640.1	231.8	570.7	49.2
3	650.4	235.5	561.6	48.8	17	626.4	226.9	583.1	49.7
4	641.3	232.2	569.6	49.2	18	617.8	223.7	591.3	50.1
5	648.4	234.8	563.4	48.9	19	610.4	221.1	598.4	50.4
6	652.3	236.2	560.0	48.7	20	620.5	224.7	588.7	50.0
7	652.7	236.4	559.7	48.7	21	602.7	218.3	606.1	50.7
8	648.3	234.8	563.5	48.9	22	590.9	214.0	618.2	51.2
9	649.8	235.3	562.2	48.8	23	583.2	211.2	626.3	51.5
10	648.8	235.0	563.0	48.9	24	596.4	216.0	612.5	51.0
11	647.6	234.5	564.1	48.9	25	571.9	207.1	638.7	52.1
12	647.8	234.6	563.9	48.9	26	554.3	200.7	659.0	52.9
13	643.0	232.9	568.1	49.1	27	531.6	192.5	687.1	54.0
14	638.3	231.2	572.2	49.3	28	560.8	203.1	651.4	52.6

Table 3.1: BINGO beams.

3.2.1 Interferometry and cross correlations

To recover the correct position of the source, the BINGO Interferometry System (BIS) will perform cross-correlations between pairs of telescopes. Assuming a perfect time delay compensation, with no taper and unity weighting function, each baseline works as an individual telescope with sensitivity given by (Walker 1989; Thompson et al. 2017)

$$S^{(0)}_{\rm min,\,i\times j} = \sqrt{\frac{S^{(0)}_{\rm min,\,i} S^{(0)}_{\rm min,\,j}}{2}}\,, \tag{3.6}$$

while the antenna pattern is equal to

$$P_{n,\,\rm i\times j}(\mathbf{n}) = \sqrt{\frac{P_{n,\,i}(\mathbf{n}) P_{n,\,j}(\mathbf{n})}{2}}\,. \tag{3.7}$$

In a typical interferometry problem, the antenna pattern must be multiplied by an interference factor ($\propto \cos(2\pi\nu\tau)$, where τ is the time delay between measurements of two telescopes). Assuming a perfect time delay measurement we can compensate it

Mirror (m)	$A_{\rm eff}$ (m^2)	G (mK/Jy)	$S^{(0)}_{\rm min}$ (mJy)	$\theta_{1/2}$ (arcmin)
-	1.5	0.5	251.8	1034.1
4	9.8	3.6	37.1	396.9
5	15.4	5.6	23.8	317.5
6	22.9	8.3	15.9	259.9

Table 3.2: Outrigger types.

by substituting $\cos(2\pi\nu\tau)$ by $\cos(2\pi\nu(\tau - \tau_{\rm obs}))$; this procedure is called time delay compensation and assuming that we can always set $\tau = \tau_{\rm obs}$ the cosine becomes equal to one reducing to the form in Eq. (3.7).

The total directional sensitivity for a set of N telescopes is given by (Walker 1989)

$$\frac{1}{S^2_{\rm min}(\mathbf{n})} = \sum_{i=1}^{N} \frac{1}{S^2_{\rm min,\,i}(\mathbf{n})} + \sum_{i=1}^{N-1} \sum_{j=i+1}^{N} \frac{X_{ij}}{S^2_{\rm min,\,i\times j}(\mathbf{n})}, \tag{3.8}$$

where $X_{ij} = 1$ if the telescopes i and j are physically correlated, or $X_{ij} = 0$ if they are not.

3.3 Generating synthetic FRBs

To estimate the number of detections and localizations, we need to produce reliable mock catalogs. Data in the synthetic catalog contain several physical quantities randomly generated, following a probability distribution function (PDF) chosen by the user. In this section, I will detail each of the physical quantities, following Luo et al.; Luo et al. (2018; 2020) and present `FRBlip`, a `Python` code developed for this work. Our simulations consider only non-repeaters and extragalactic FRBs.

For the single i-th FRB the observed signal-to-noise (S/N) ratio, measured by a telescope of directional sensitivity $S_{\rm min}(\mathbf{n})$, is given by

$$(S/N)_i = \frac{S_{\rm peak,\,i}}{S_{\rm min}(\mathbf{n}_i)}, \tag{3.9}$$

where $S_{\rm peak}$ is the peak density flux, given by (Lorimer et al. 2013)

$$S_{\rm peak} = \frac{L_{\rm bol}}{4\pi d_L(z)^2} \frac{(1+z)^{\alpha+1}}{\nu'^{\alpha+1}_{\rm high} - \nu'^{\alpha+1}_{\rm low}} \left(\frac{\nu_2^{\alpha+1} - \nu_1^{\alpha+1}}{\nu_2 - \nu_1} \right) , \tag{3.10}$$

where $d_L(z)$ is the luminosity distance, $L_{\rm bol}$ the bolometric luminosity, α the spectral index, ν_1 and ν_2 the observed frequencies. $\nu'_{\rm low}$ and $\nu'_{\rm high}$ are the lowest and highest frequencies over which the source emits, respectively, in the rest-frame of the source. This restriction on the emission frequencies implies a range of redshift given by

$$z_{\rm min} = \max \left[0, \frac{\nu'_{\rm low}}{\nu_2} - 1 \right] \tag{3.11}$$

and

$$z_{\rm max} = \frac{\nu'_{\rm high}}{\nu_1} - 1 \, . \tag{3.12}$$

I use the results presented in Luo et al. (2020) to generate the FRBs, where the constraints on the free parameters of the luminosity function were obtained assuming a flat spectrum with intrinsic spectral width $\Delta\nu_0 = \nu_{\rm Luo,\,high} - \nu_{\rm Luo,\,low} = 1$ GHz. Given that the spectrum is restricted to this specific band, the corresponding luminosity is not, strictly speaking, a bolometric luminosity. Therefore, as presented in appendix A, the peak flux density that we will use is

$$S_{\rm peak} = \frac{L}{4\pi d_L(z)^2} \frac{1}{\nu^{\alpha+1}_{\rm Luo,\,high} - \nu^{\alpha+1}_{\rm Luo,\,low}} \left(\frac{\nu_2^{\alpha+1} - \nu_1^{\alpha+1}}{\nu_2 - \nu_1} \right) , \tag{3.13}$$

where $\nu_{\rm Luo,\,high}$ and $\nu_{\rm Luo,\,low}$ are now the highest and lowest frequencies, respectively, in which the source emits as seen by the observer. While a flat spectrum was assumed in Luo et al. (2020) because of the sample of detected FRBs around 1.4 GHz used, we assume that the same distributions are valid for a general spectral index, at least between zero and -1.5. The intrinsic spectral width of 1 GHz does not contain the exact information about the frequencies $\nu_{\rm Luo,\,high}$ and $\nu_{\rm Luo,\,low}$, however, we can take values around 1.4 GHz, i.e. $\nu_{\rm Luo,\,high} = 1.4$ GHz and $\nu_{\rm Luo,\,low} = 400$ MHz. The BINGO

bandwidth is located inside this frequency interval; other intervals were investigated in the initial estimates presented in Abdalla et al. (2022a).

From Eq. (3.8) we conclude that the total S/N is given by:

$$\text{Total}[S/N] = \sqrt{\text{Auto}[S/N]^2 + \text{Intf}[S/N]^2}\,, \tag{3.14}$$

where Auto$[S/N]$ is the total auto-correlation signal-to-noise ratio

$$\text{Auto}[S/N] = \sqrt{\sum_{i=1}^{N} (S/N)_i^2}\,, \tag{3.15}$$

and Intf$[S/N]$ is the total cross-correlation signal-to-noise ratio, given by

$$\text{Intf}[S/N] = \sqrt{\sum_{i=1}^{N-1} \sum_{j=i+1}^{N} X_{ij} (S/N)_{i\times j}^2}\,. \tag{3.16}$$

Therefore, the intrinsic quantities which must be simulated are z, L, α, and $\mathbf{n}$.

3.3.1 Cosmological population

Redshift distribution

The FRB spatial distribution is not known yet due to the small number of measured redshifts of the associated host galaxy (Heintz et al. 2020). Some redshift distributions for FRBs have been considered over the years, e.g. a Poisson distribution $P(z) = ze^{-z}$ motivated by the distribution of gamma-ray bursts (Zhou et al. 2014; Yang & Zhang 2016) or a redshift distribution following the galaxy distribution $P(z) = z^2 e^{-\beta z}$ (Hagstotz et al. 2022). The alternative possibility used here is a spatial distribution uniform in comoving volume (Luo et al. 2018; Chawla et al. 2022)

$$f_z(z) \equiv \frac{\partial V}{\partial \Omega \partial z} = \frac{c}{1+z} \frac{r^2(z)}{H(z)}\,, \tag{3.17}$$

where $\partial V/(\partial\Omega\partial z)$ is the differential comoving volume per unit solid angle per unit redshift, c is the speed of light, $r(z)$ is the comoving distance, and

$$H(z) = H_0\sqrt{\Omega_m(1+z)^3 + \Omega_\Lambda} \tag{3.18}$$

is the parameterized version of the first Friedmann-Lemaître equation. We use the best-fit values from the Planck collaboration (Aghanim et al. 2020) for the matter density parameter, $\Omega_m = 0.31$, dark energy density parameter, $\Omega_\Lambda = 0.69$, and Hubble constant today, $H_0 = 67.4$ km/s/Mpc. The term $(1+z)$ takes into account the time dilation due to the cosmic expansion. The redshift is sampled according to the distribution in Eq. (3.17) for up to the maximum value of $z_{\max} = 10$.

3.3.2 Luminosity distribution

The luminosity function of FRBs is also still not well understood and although lognormal or power-law distributions have previously been used (Caleb et al. 2016), the Schechter function (Schechter 1976) opted in Luo et al.; Luo et al. (2018; 2020) seems to be favored over the others (Petroff et al. 2019b). Thus, we assume here that it is given by

$$\phi(L) = \phi^\star \left(\frac{L}{L^\star}\right)^\gamma e^{-L/L^\star}, \tag{3.19}$$

where $L^\star$ is the upper cut-off luminosity, $\phi^\star$ is a normalization constant and γ is the power-law index. These parameters were constrained in Luo et al. (2020) using 46 FRBs: $L^* = 2.9 \times 10^{44}$erg s^{-1}, $\phi^* = 339$ Gpc^{-3}yr^{-1} and $\gamma = -1.79$.

Spectral index

The flux density of FRBs depends on the frequency as $S_\nu \propto \nu^\alpha$, where the spectral index α can be positive or negative. In Luo et al. (2020) $\alpha = 0$ was chosen inspired by the apparently flat spectrum of FRB 121102 with 1 GHz of bandwidth (Gajjar et al. 2018b). Chawla et al. (2017) reported a lack of FRB observations in the Green

Bank Northern Celestial Cap survey at 350 MHz, indicating either a flat spectrum or a spectral turnover at frequencies above 400 MHz. However, some works (e.g. Lorimer et al. 2013) have assumed a spectral index similar to the one observed in pulsars ($\alpha = -1.4$; Bates et al. 2013). Such value is very close to the result obtained by Macquart et al. (2019b) using 23 FRBs ($\alpha = -1.5$). Based on these previous works, we choose here to use two different values for the spectral index, $\alpha = 0$ and $\alpha = -1.5$. Similar values are also used in `frbpoppy` in its different population setups (Gardenier et al. 2019).

Number of sources

Several estimates of the all-sky rate of observable FRBs have been made. For instance, Thornton et al. (2013) estimated a rate of 10^4 sky^{-1}day^{-1} above a fluence of 3 Jy ms, while CHIME recently inferred a sky rate of 820 sky^{-1}day^{-1} above a fluence of 5 Jy ms at 600 MHz (Amiri et al. 2021). Luo et al. (2020) found event rate densities of 3.5×10^4 Gpc^{-3} yr^{-1} above a luminosity of 10^{42} erg s^{-1}, 5.0×10^3 Gpc^{-3} yr^{-1} above 10^{43} erg s^{-1} and 3.7×10^2 Gpc^{-3} yr^{-1} above 10^{44} erg s^{-1}. We estimate the rate per day per sky of detectable FRBs using the following expression (Luo et al. 2020)

$$\lambda = 4\pi \int_0^\infty f_z(z)\,\mathrm{d}z \int_{L_0}^\infty \phi(L)\,\mathrm{d}L\,, \tag{3.20}$$

where $f_z(z)$ and $\phi(\log L)$ are given by Equations (3.17) and (3.19), respectively, and L_0 is the intrinsic lower cut-off of the luminosity function inferred to be $\leq 9.1 \times 10^{41}$ erg s^{-1}. Using Eq. (3.20) with the values of the minimum flux density and observed pulse width for BINGO described in the next section, we estimate the total number of cosmic FRBs to be generated by `FRBlip` to be $\sim 7 \times 10^4$ per day of observation. In the next sections, we will describe the methodology used to estimate the detection rate for BINGO, which will be a fraction of this cosmic population.

3.3.3 Sensitivity Maps

The simplest way to estimate the detection rate is is to follow the approach adopted by(Luo et al. 2020), also used in Abdalla et al. (2022a), through the equation

$$\lambda_\alpha(\mathbf{n}) = \int_{z_{\min}}^{z_{\max}} f_z(z)\,\mathrm{d}z \int_{L_{\min}(z,\mathbf{n})}^{\infty} \phi(L)\,\mathrm{d}L\,. \tag{3.21}$$

The difference between Equations (3.20) and (3.21) is that the former assumes an all-sky rate, while the latter is going to be calculated for the BINGO field-of-view and for redshift values bounded by the frequency range.

The minimum luminosity $L_{\min}$ in the lower limit of integration is the maximum function $\max[L_0, L_{\mathrm{thre}}]$, where L_{thre} depends on the spectral index α and the antenna pattern

$$L_{\mathrm{thre}}(z,\mathbf{n}) = 4\pi d_L(z)^2 \Delta\nu \left(\frac{\nu_{\mathrm{Luo,high}}^{\alpha+1} - \nu_{\mathrm{Luo,low}}^{\alpha+1}}{\nu_2^{\alpha+1} - \nu_1^{\alpha+1}} \right) (\mathrm{S/N})\, S_{\min}(\mathbf{n})\,, \tag{3.22}$$

where $\Delta\nu = \nu_2 - \nu_1$ and $S_{\min}$ is the telescope minimum flux density defined in eq. 3.5). The detection rate per unit of time is found integrating over the telescope field-of-view

$$\lambda_\alpha = \int_{S^2} \lambda_\alpha(\mathbf{n})\mathrm{d}\Omega\,, \tag{3.23}$$

where this angular integration is performed using `HEALPix` (Górski et al. 2005), through `astropy-healpix` (Price-Whelan et al. 2018)

$$\lambda_\alpha = \Omega_{\mathrm{pix}} \sum_{i=1}^{n_{\mathrm{pix}}} \lambda_\alpha(\mathbf{n}_i)\,, \tag{3.24}$$

where n_{pix} and Ω_{pix} depend on the resolution (n_{side}) of the `HEALPix` map. Detection rate estimates for the BINGO configurations described previously are shown in Fig. 4.4. The limitation of the present approach lies in the fact that computing complex quantities as the observation rates over the baselines is very costly. Indeed, to compute

the detection rate of at least two baselines, we have to compute the sensitivity map for all the possible pairs of baselines. For three baselines we must compute it for all possible combinations of three baselines and so on.

3.3.4 FRBlip

To compute all quantities described in previous sections, we developed `FRBlip`[2], a new `Python` package which generates mock catalogs sorting the physical quantities as random numbers, through the distributions described in section 3.3.1. The information about the cosmic population is coded inside an object called `FastRadioBursts`, and the telescopes in objects of the type `RadioTelescope`. The results of observations come from the interaction between these two entities.

The dependencies of the `FRBlip` include traditional `Python` numerical libraries such as `Numpy` (Harris et al. 2020), `Scipy` (Virtanen et al. 2020) and `Pandas` (pandas development team 2020); high performance collection libraries as `Xarray` (Hoyer & Hamman 2017) and `Sparse`; the physical numerical libraries `astropy` (Price-Whelan et al. 2018), `HEALpix` (Górski et al. 2005) and `Pygedm` (Price et al. 2021); and the numerical computing packages for cosmology: `CAMB` (Lewis & Bridle 2002), and `PyCCL` (Chisari et al. 2019).

[2] www.github.com/mvsantosdev/frblip

Chapter 4

Results

4.1 Detecting Bursts

We evaluate here a more accurate detection rate. For that, we generated cosmological FRB mock catalogs and counted how many of those would be detected by the main BINGO, the outriggers, and the total BIS in different scenarios. The key quantity is the yearly rate.

The FRB mock catalogs were produced by first generating one day of cosmological FRBs, then re-sampling the 1-day mock 365 times, to create a catalog for one year of observations, but with sky positions (right ascension and declination) fixed. This procedure is then repeated 1000 times until we have enough data to adequately fit a Poisson distribution, which we did by using the `statsmodels` library (Seabold & Perktold 2010).

We first investigate the detectability of individual telescopes. In Fig. 4.1 we show the redshift distribution of the FRBs seen by the main BINGO alone ($S/N \geq 1$) during five years (purple histogram) compared with all the FRBs in the sky in one day (gray histogram). This histogram is also compared with the exact distribution (purple continuous curve), computed from the sensitivity maps (3.24). We can see that the histogram is well bounded inside the 95% confidence level (C.L.) (represented by the

purple-shaded region). The red dashed line is the power log-normal[1] distribution fitted on the complete 1000 years of simulation, which is in good agreement with the exact value by 95% C.L.

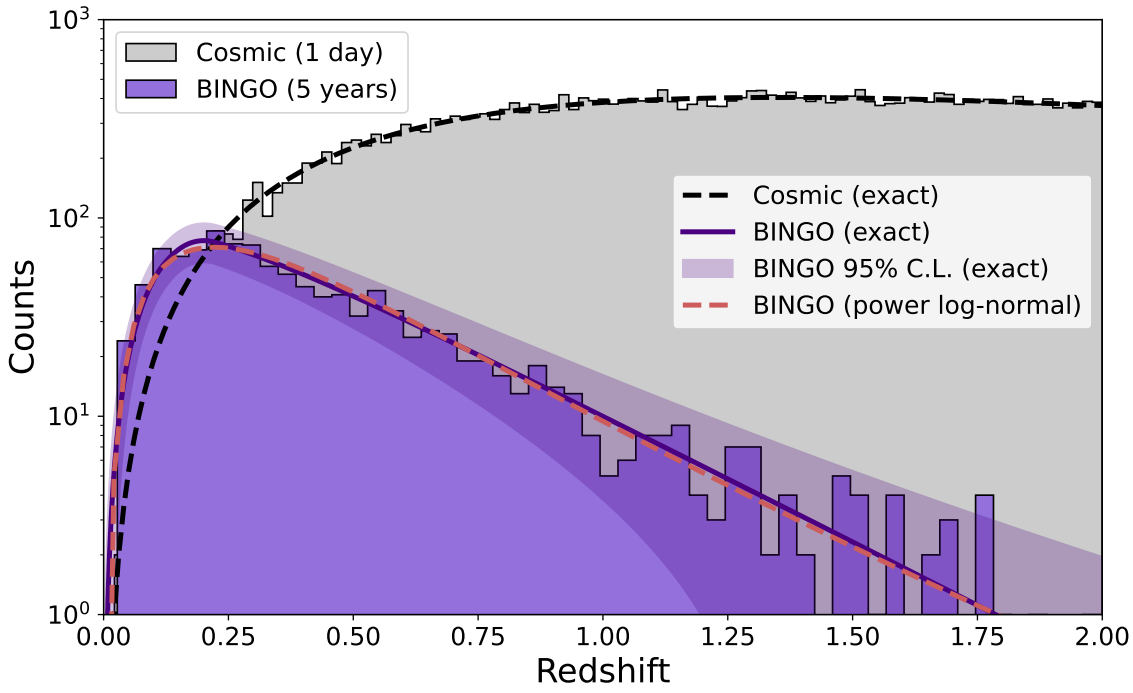

Figure 4.1: Redshift distribution of the observed FRBs, with $S/N \geq 1$, by BINGO in five years (purple histogram) compared with all the cosmic bursts in one day (grey histogram). The exact cosmic distribution is the black dashed line, the exact distribution for the BINGO is the solid purple distribution, and the shaded region is the exact 95% C.L. from the Poisson distribution. The red dashed line is the power log-normal distribution fitted from 1000 years of observation mock.

The number of FRBs increases with the redshift since the volume also increases until it reaches a maximum value. After that, it starts decreasing because the luminosity limit starts dominating. It reaches a maximum value at $z \simeq 1.8$, where the rate becomes smaller than one. Therefore, we can interpret $z = 1.8 = z_{\rm max}^{\rm eff}$, the maximum effective redshift or the depth of the survey.

Fig. 4.2 shows how the detection rate of FRBs varies with the S/N for the different telescope configurations described in Section 3.2. In all cases, we see that the $z_{\rm max}^{\rm eff}$ values inferred from the power log-normal distribution, fitted from the mocks, are in

[1] docs.scipy.org/doc/scipy/reference/generated/scipy.stats.powerlognorm.html

agreement with the exact value by 95% C.L. This alternative method to infer $z_{\max}^{\text{eff}}$ is important to determine the depth of the survey since we can not compute the exact values from sensitivity maps as discussed in Section 3.3.3.

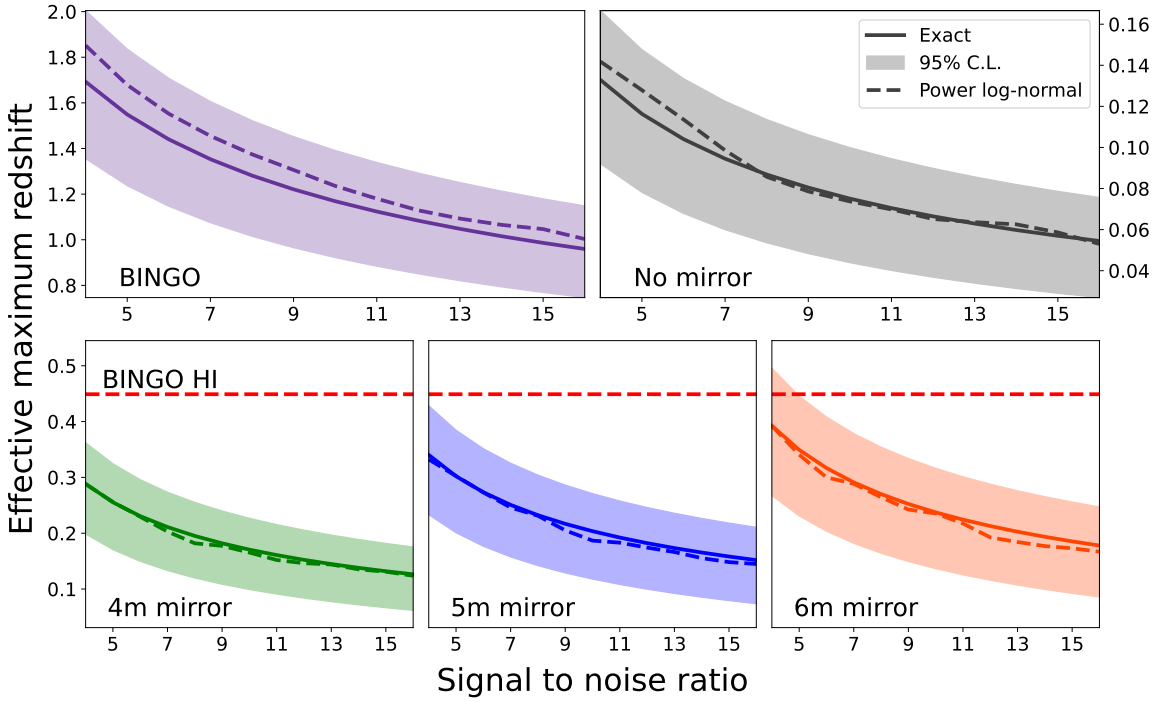

Figure 4.2: Maximum effective redshift for different BINGO configurations, varying from $S/N \geq 5$ to $S/N \geq 15$. Comparing the exact solution from sensitivity maps (solid lines), with the fitted power log-normal distribution (dashed lines), we note that all of them are in agreement with the exact solution in 95% C.L. (shaded regions). The red dashed line shows the maximum redshift of the BINGO HI survey.

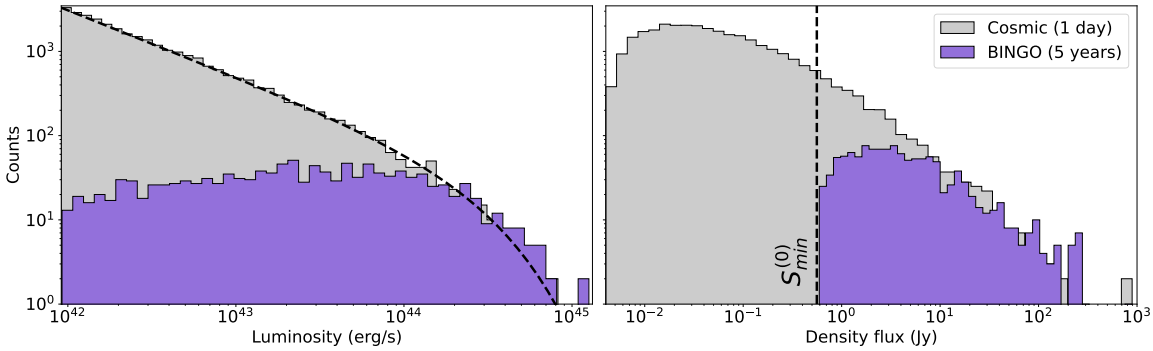

Figure 4.3: *Left*: number of events as a function of the luminosity distribution. *Right*: same, as a function of the density flux distribution. Estimates are for cosmic FBRs during 1 day (gray) and observed FRBs, with $S/N \geq 1$, during the 5 years of the BINGO Phase 1 mission (purple).

In Fig. 4.3 we show the luminosity (left) and density flux (right) distributions. Fainter objects are more difficult to observe, as expected because it is more probable to have a density flux smaller than the minimum $S_{\rm min}^{(0)}$. In order to illustrate the fraction of the distributions observed by BINGO, we compare the histograms of the cosmic distributions in one day with the ones observed by BINGO in 5 years.

Finally, we show in Fig. 4.4 the detection rates obtained from mocks and the ones computed by the sensitivity maps, evidencing the agreement between the methods. The rates from individual outriggers (top panel) are less than one per year, however, the interferometry system, which integrates nine of these telescopes, can increase the BINGO detection rate by about 20%. For the case of interferometry, we have not computed the exact distributions, due to the reasons discussed at the end of Section 3.3.3. Thus, we need an alternative method to infer the depth of these interferometric cases.

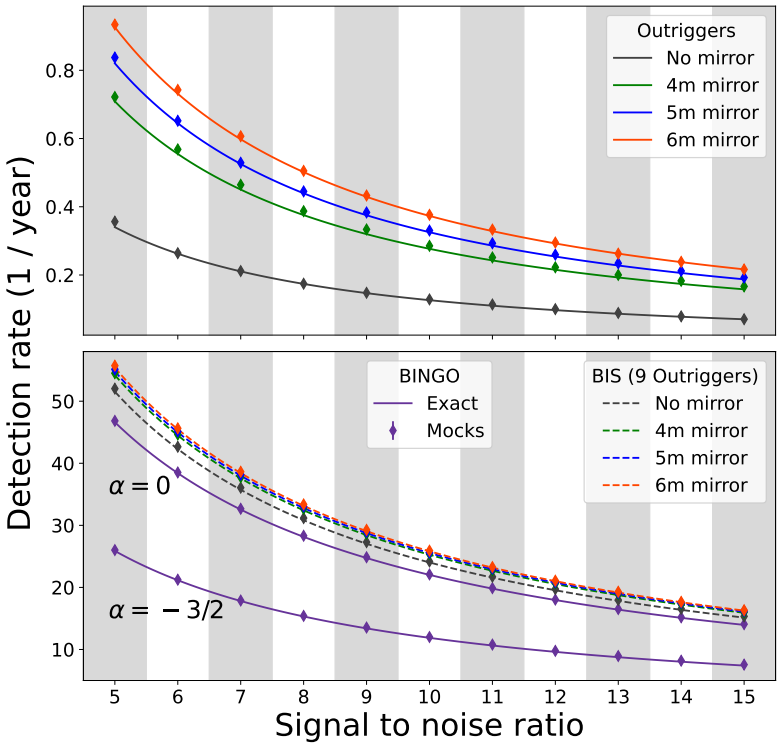

Figure 4.4: Detection rate estimates for BINGO. *Top*: mean detection rate for individual outriggers with configuration as described in Sec. 3.2 and Table 3.2. *Bottom*: detection rate for the complete BIS (main BINGO and outriggers). In both cases, we show the detection rates computed by the two methods: sensitivity maps (solid lines) and mock catalogs created with `FRBlip` (scatter).

4.2 Localizing Bursts

We now evaluate the effectiveness of BIS to localize FRBs. We assume a perfect delay compensation, i.e., the exact time delay between the telescopes that compose each baseline is known. In this case, the accuracy of localizing an FRB increases with the number of baselines that are used to observe it. Therefore, we have to select the better BIS configuration between the two options: more outriggers with narrower beam widths or fewer outriggers with wider beam widths.

The number of FRBs detected by different baselines depends on the number of outriggers used in the system and the size of the mirror. In Fig. 4.5 we show the fraction of FRBs (with respect to the total BIS detections) observed by one, two, or three baselines, varying with S/N, for different numbers of outriggers. While the number of outriggers has a direct impact on the fraction of detected FRBs (i.e. more outriggers increase the fraction of detected events), the mirror size does not play a straightforward role in this fraction. In some situations, the larger the mirror the greater the fraction of detected FRBs (a localization using one baseline for 5, 7, 9, or 10 outriggers). However, for localization using two baselines, smaller mirrors produce better results (for 5 and 7 outriggers the best scenario is with a 4-m mirror, while for 9 (10) outriggers the best choice is a 5-m (6-m) mirror. For localization using three baselines, a naked horn is the best choice for 5 outriggers, while a horn with a 4-m mirror is better for 7, 9, and 10 outriggers. Ultimately, the choice of mirror size will depend on the number of outriggers built and on the number of baselines needed to detect the same FRB.

These results are not enough to decide which is the best configuration for a BIS composed only of single-horn outriggers. To accurately answer this question we must define the following points: (i) by how many baselines an FRB must be observed to have its position well inferred; (ii) how many outriggers we can construct; and (iii) which kind of outriggers will be constructed.

The answer to the first question depends only on how effective is the pipeline to

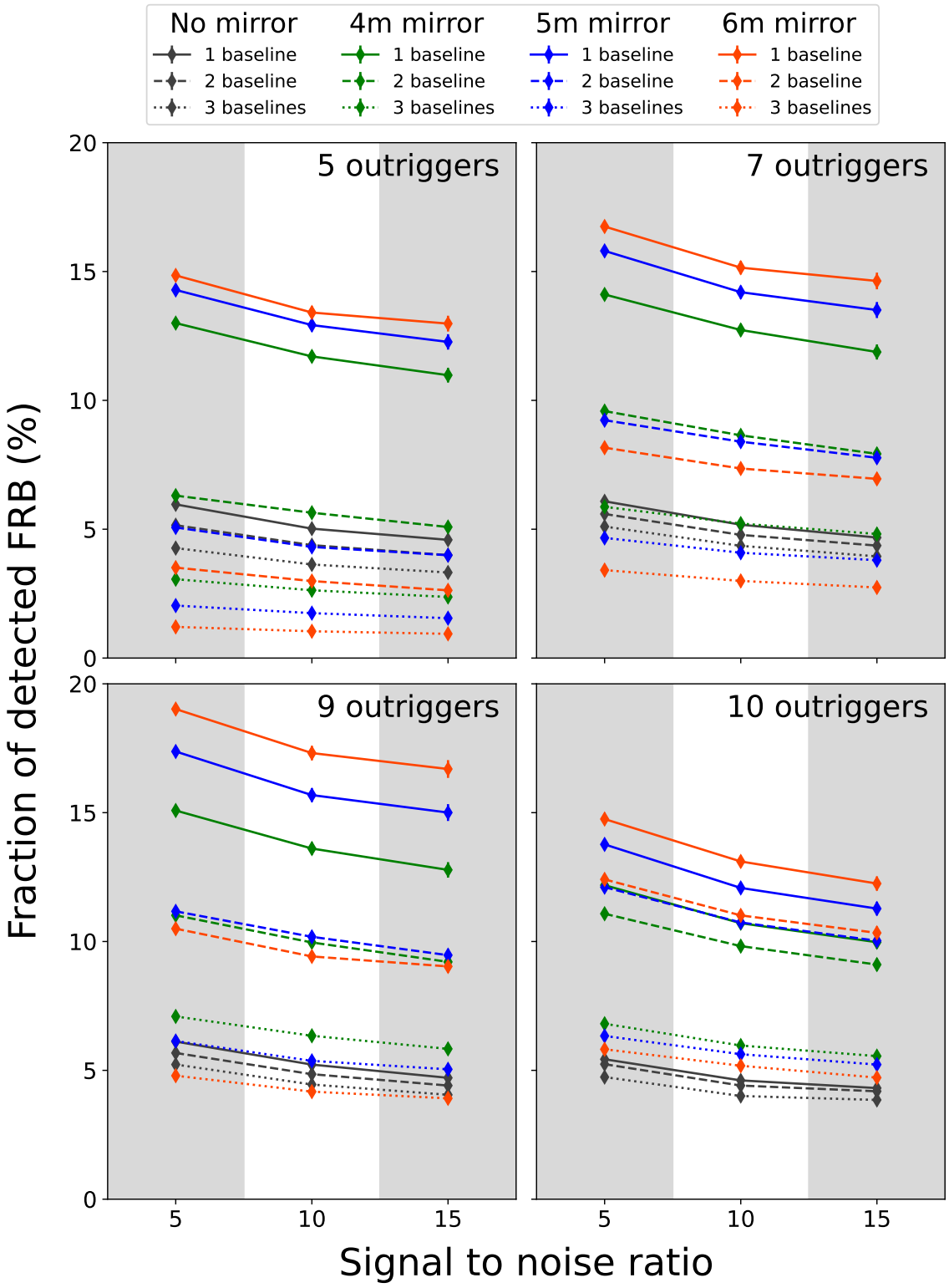

Figure 4.5: Fraction of observed FRBs (by BIS) by one, two, or three baselines for $S/N \geq 5$, $S/N \geq 10$, and $S/N \geq 15$, for the sixteen different BIS configurations.

infer the positions. Assuming that a minimum of two baselines is enough to pinpoint the source position, from Fig. 4.6 we may infer the best type of outrigger for each configuration.

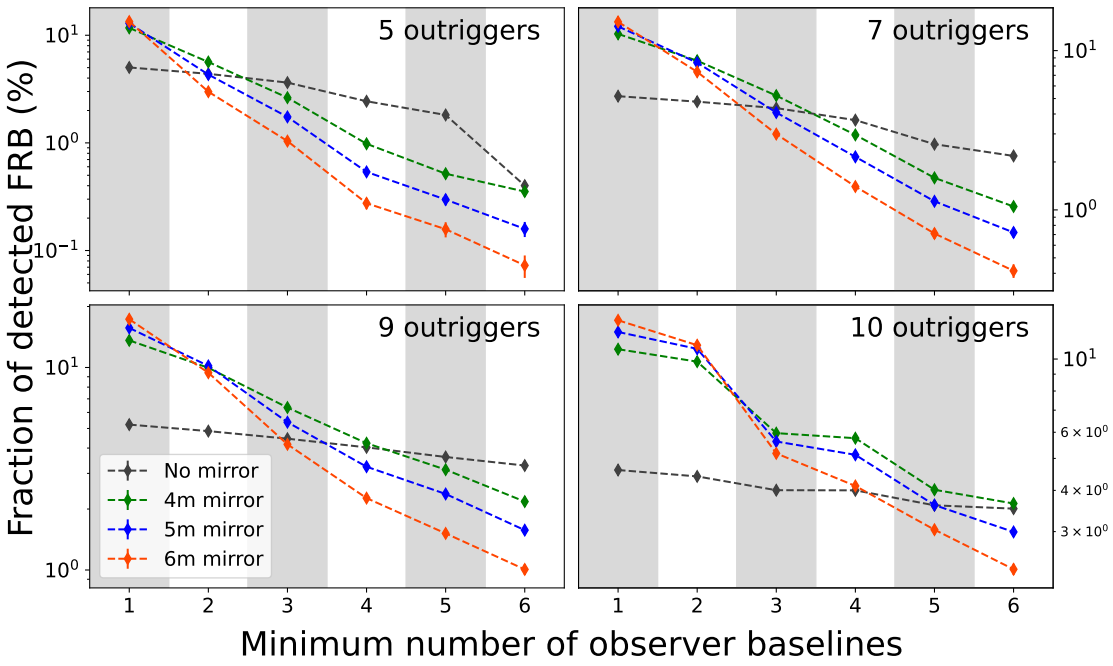

Figure 4.6: The fraction of observed bursts ($S/N \geq 10$) as a function of baselines that detected the same events, for the sixteen different BIS configurations.

For 5 outriggers, the best choice is the 4 m mirror, for 7 outriggers the performance of 4 m and 5 m mirrors are almost the same, for 9 outriggers 4 m, 5 m, and 6 m perform approximately equal, and for 10 outriggers the 6 m mirror is the best. If we make it more restrictive, requiring at least 3 baselines the picture changes a bit. For 5 outriggers, for instance, now the horn with no mirror performs best, while for the other configurations (7, 9, and 10 outriggers), the 4-m mirror produces the best result.

The number of outriggers would also depend on the number of baselines needed to permit a good localization of the source. In order to understand how the number of detections per baseline affects our results, we show in Fig. 4.6 the fraction of detected FRBs as a function of the number of baselines that detected a given FRB. We set the S/N to ten or higher. For this illustrative choice of S/N, we see that the fraction of detected FRBs follows the same behavior in all 4 different panels. The outriggers

with a 4-m size detect more (or at least the same number) events than the ones with larger mirrors, with the exception of 10 outriggers with two baselines. However, if more baselines detect the same FRB, then the naked horn is the best option for 5 or 7 outriggers, that is, for 5 outriggers the naked horn is better if the detections are made by three baselines or more, for 7 outriggers the naked horn is better if the detections are made by four baselines or more, and so forth.

So far we have estimated the detection rates considering that the baselines and the auto-correlations have the same S/N threshold. However, this choice is arbitrary and we may set a different approach, for instance, to first select a group of candidates observed by the main BINGO, and then filter this group with a different choice of S/N to define a detection in a baseline. In order to investigate how these different choices affect our results, we defined a set of values for the S/N that will categorize an FRB as a candidate, a detection, an interferometry detection (for the cross-correlation between main BINGO and outriggers), and localizations in one, two or three baselines. This set of definitions is shown in Table 4.1.

Label	Condition
Candidate	If a given event has $S/N \geq s_1$, either for auto or cross-correlations
Detection	Candidate with Total$[S/N] \geq s_2$
Interferometric detection	Detection with Intf$[S/N] \geq s_3$
Localization/Baselines	Number of baselines that observed the same FRB satisfying $S/N \geq s_4$ for an interferometry detection

Table 4.1: $s_1 = 2$, $s_2 = 5$, $s_3 = 3$, and $s_4 = 2$.

In Table 4.1, the condition s_1, corresponding to the label "Candidates" and S/N ≥ 1, is chosen to select the events that might be an actual FRB detection. Such S/N does not need to be much larger than 1 and can occur either in auto or cross-correlation since at this level we are simply looking for at least one baseline that received a potential signal. For the label "Detection" (meaning an actual detection), we choose $s_2 = 5$ in order to pick candidates that certainly would be detected by the telescope. The

same occurs for s_3 in the interferometric detection, although in this step we already know that a detection occurred. Here we are selecting $s_3 = 3$ because we are interested in knowing if the FRBs would be clearly detected in interferometry nide, aiming to pinpoint the source location. To precisely locate the FRB in the sky we need that each baseline has a considerable S/N value per event, and for this, we have selected $s_4 = 2$.

In Table 4.2 and in the top panel of Fig. 4.7 we show the results for the categorization described in Table 4.1.

Number of Outriggers	Mirror size (m)	Candidates	Detections	Interferometry Detections	Localizations for Baselines 1	2	3
5	No dish	121.5	49.5	11.5	9.5	8.3	6.9
	4	124.7	50.9	16.3	19.9	10.3	5.0
	5	125.8	51.3	16.5	21.7	8.2	3.5
	6	126.9	51.7	16.2	22.3	5.8	2.1
7	No dish	121.5	50.7	14.2	10.0	9.2	8.4
	4	125.1	52.7	21.7	22.1	15.9	9.9
	5	126.6	53.2	22.0	24.5	15.3	8.0
	6	128.2	53.7	21.6	25.7	13.6	6.0
9	No dish	121.6	52.0	16.5	10.2	9.5	8.8
	4	126.1	54.5	25.9	24.3	18.4	12.3
	5	128.0	55.1	26.7	27.7	18.8	10.7
	6	130.4	55.7	26.5	29.9	17.8	8.6
10	No dish	119.2	52.3	17.2	9.7	9.3	8.5
	4	121.7	55.3	26.9	21.7	20.1	12.5
	5	122.9	56.0	28.0	24.3	22.0	11.9
	6	124.2	56.6	28.3	25.7	22.6	11.1

Table 4.2: (*) $\alpha = -1.5$. Observation rates (per year) for categorization are described in Table 4.1. Each set of outriggers (5, 7, 9, or 10) has four options of mirrors. The last three columns present the number of FRBs detected simultaneously (and named here as 'localizations') by a different number of baselines.

The number of candidates increases slightly with the increase in the number of outriggers and mirror sizes. On the other hand, the number of detections, interferometric detections, and localizations using one baseline increases considerably with the number of outriggers and mirror sizes. The localizations using two or three baselines, however, are almost in all cases larger for a 4-m mirror with 5, 7, or 9 outriggers. The number of localizations for a specific mirror size roughly increases with the number of outriggers. However this does not mean always an increase in coverage area and the exception is the scenario with 10 outriggers, where there are many overlaps between the outriggers'

beams and main BINGO's (as can be seen from Fig. 3.12), thus in practice the total observed area is less than the area of the scenario with 5 outriggers case.

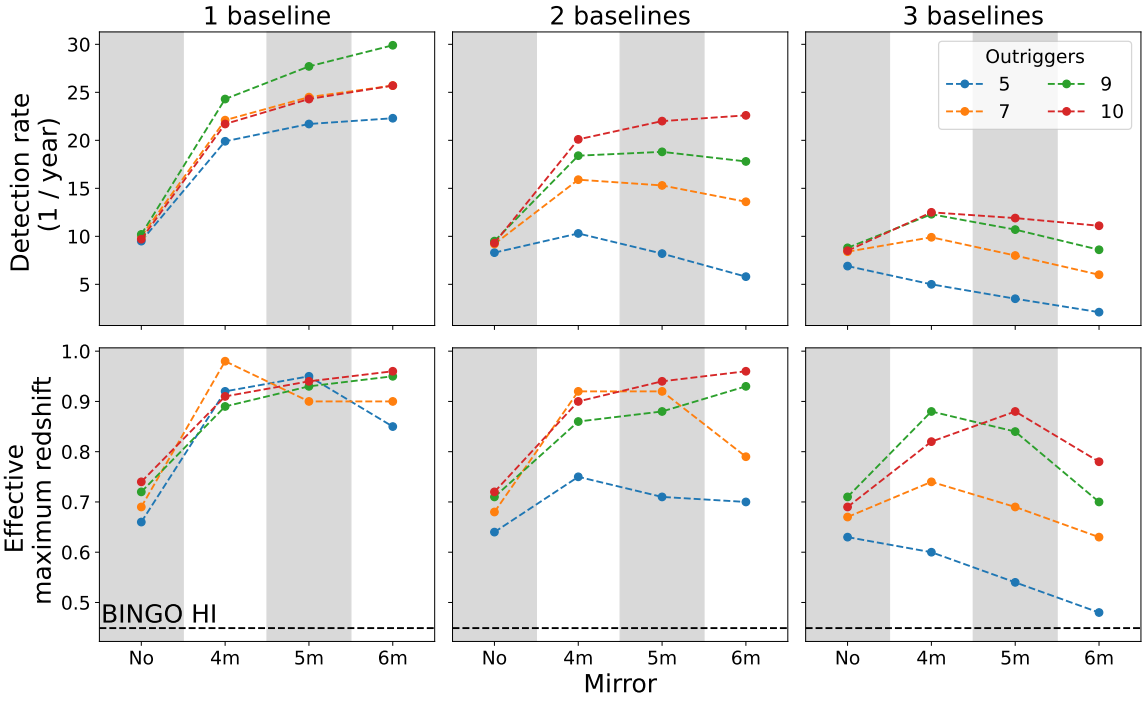

Figure 4.7: Yearly detection rate (top) and effective maximum redshift (bottom), for prescription described in Table 4.1, as a function of the mirror size for 5, 7, 9, and 10 outriggers.

As it can be seen in Table 4.3 and bottom panel of Fig. 4.7, the effective maximum redshift is between 2 and 3 for candidates and detections, but it is reduced to generally $0.5 - 1$ for the localization.

We conclude from this analysis that narrow beams, i.e. horns with bigger mirrors, can observe higher redshift values but an FRB can be observed by more beams with a set composed of larger beams. This problem is compensated for by introducing more telescopes to the BIS, which expands the observed area.

As can be seen in Table 4.2, the introduction of more outriggers can multiply by many factors the detection rates. Regarding the localizations, the performance saturates for 1, 2, or 3 baselines, reaching hundreds of localized bursts. We see similar behavior in Table 4.3 for the redshift, where the outriggers improve the depth of the survey.

Number of Outriggers	Mirror size (m)	Candidates	Detections	Interferometry Detections	Baselines 1	2	3
5	No dish	2.40	2.08	0.67	0.66	0.64	0.63
	4	2.43	2.12	0.89	0.92	0.75	0.60
	5	2.44	2.25	0.91	0.95	0.71	0.54
	6	2.45	2.13	0.81	0.85	0.70	0.48
7	No dish	2.40	2.08	0.73	0.69	0.68	0.67
	4	2.43	2.13	0.98	0.98	0.92	0.74
	5	2.44	2.13	0.88	0.90	0.92	0.69
	6	2.45	2.14	0.88	0.90	0.79	0.63
9	No dish	2.39	2.12	0.77	0.72	0.71	0.71
	4	2.43	2.14	0.89	0.89	0.86	0.88
	5	2.68	2.14	0.92	0.93	0.88	0.84
	6	2.46	2.15	0.93	0.95	0.93	0.70
10	No dish	2.37	2.08	0.79	0.74	0.72	0.69
	4	2.40	2.11	0.93	0.91	0.90	0.82
	5	2.40	2.11	0.95	0.94	0.94	0.88
	6	2.41	2.12	0.99	0.96	0.96	0.78

Table 4.3: (*) $\alpha = -1.5$. Similar to Table 4.2 but now presenting the effective maximum redshift ($z_{\rm max}^{\rm eff}$) from power log-normal distribution, for the categorization described in Table 4.1.

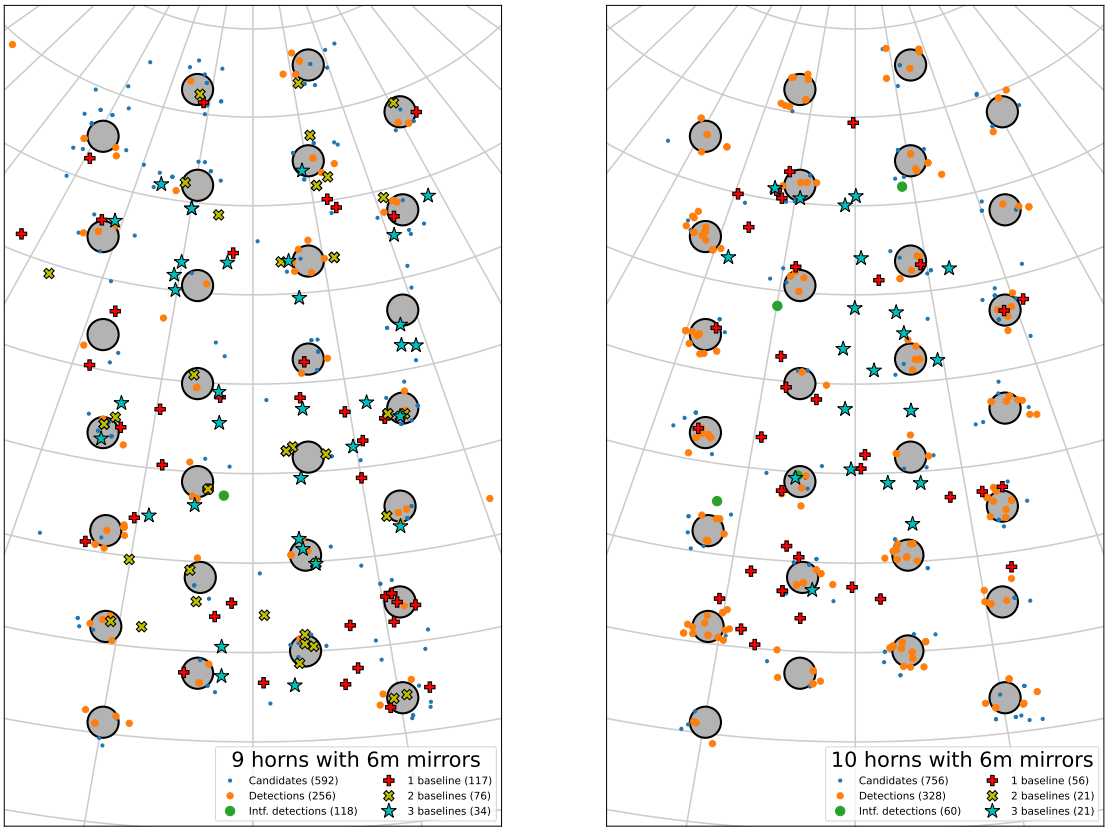

Figure 4.8: Distribution of candidates and detections for two outrigger configurations.

Chapter 5

Final Remarks

In this dissertation I have investigated the performance of the BINGO telescope to search and detect FRBs, and how a set of outriggers can be used to localize the events in the sky, through the BIS. I considered a single, naked horn plus three different mirror sizes for the outriggers, all with single horns, for 5, 7, 9, and 10 outriggers. To produce synthetic FRBs and calculate the detection rates, I used and helped to develop the code `FRBlip`.

Using different methodologies to define detection and localization through baselines, I estimate that BINGO alone will be able to observe dozens of FRB per year, around 50 with $S/N \geq 5$ and 20 with $S/N \geq 15$ (for $\alpha = 0$, as used in Eq. 3.22), in agreement to what was previously calculated in Abdalla et al. (2022a). The introduction of outriggers can improve the total detection rate by about 20% with 9 outriggers (as can be seen in Fig. 4.5).

Regarding the localization, if we use two baselines then the best scenario is when outriggers have a 4-m mirror, and the estimates are improved from 10.3 events per year (for 5 outriggers) to 15.9 events per year (for 7 outriggers), 18.4 events per year (for 9 outriggers) or 20.1 events/year (for 10 outriggers), as seen in Table 4.2. On the other hand, if the localization is through three baselines, the best case is for 7, 9, or 10 outriggers with a 4-m mirror, with $10 - 12.5$ events per year; with 5 outriggers, the best option would be outriggers without mirrors, reaching 7 events per year.

Bibliography

Abdalla, E. et al. 2022a, Astron. Astrophys., 664, A14

Abdalla, F. B. et al. 2022b, Astron. Astrophys., 664, A16

Aghanim, N. et al. 2020, Astron. Astrophys., 641, A6, [Erratum: Astron.Astrophys. 652, C4 (2021)]

Amiri, M. et al. 2018, arXiv reprint:astro-ph, 1803.11235

Amiri, M. et al. 2021, Astrophys. J. Supp., 257, 59

Bagchi, M. 2017, The Astrophysical Journal Letters, 838, L16

Bailes, M., Jameson, A., Flynn, C., et al. 2017, PASA, 34, e045

Bannister, K. W., Deller, A. T., Phillips, C., et al. 2019, Science, 365, 565

Bassa, C., Tendulkar, S., Adams, E., et al. 2017, The Astrophysical Journal Letters, 843, L8

Bates, S. D., Lorimer, D. R., & Verbiest, J. P. W. 2013, Mon. Not. Roy. Astron. Soc., 431, 1352

Beloborodov, A. M. 2017, The Astrophysical Journal Letters, 843, L26

Beloborodov, A. M. 2020, The Astrophysical Journal, 896, 142

Bhandari, S., Keane, E., Barr, E., et al. 2018, Monthly Notices of the Royal Astronomical Society, 475, 1427

Bhandari, S., Sadler, E. M., Prochaska, J. X., et al. 2020, The Astrophysical Journal Letters, 895, L37

Bhandari, S. et al. 2022, Astron. J., 163, 69

Bharadwaj, S. & Sethi, S. K. 2001, J. Astrophys. Astron., 22, 293

Caleb, M., Flynn, C., Bailes, M., et al. 2016, Mon. Not. Roy. Astron. Soc., 458, 708

Caleb, M., Flynn, C., & Stappers, B. 2019, Monthly Notices of the Royal Astronomical

Society, 485, 2281

Caleb, M., Stappers, B., Abbott, T., et al. 2020, Monthly Notices of the Royal Astronomical Society, 496, 4565

Champion, D. J., Petroff, E., Kramer, M., et al. 2016, Monthly Notices of the Royal Astronomical Society: Letters, 460, L30

Chatterjee, S., Law, C., Wharton, R., et al. 2017, Nature, 541, 58

Chawla, P., Andersen, B. C., Bhardwaj, M., et al. 2020, The Astrophysical Journal Letters, 896, L41

Chawla, P., Kaspi, V. M., Josephy, A., et al. 2017, ApJ, 844, 140

Chawla, P. et al. 2022, Astrophys. J., 927, 35

Chisari, N. E. et al. 2019, Astrophys. J. Suppl., 242, 2

Chittidi, J. S., Simha, S., Mannings, A., et al. 2021, The Astrophysical Journal, 922, 173

Connor, L., Sievers, J., & Pen, U.-L. 2016, Monthly Notices of the Royal Astronomical Society: Letters, 458, L19

Cordes, J. M. & Chatterjee, S. 2019, Ann. Rev. Astron. Astrophys., 57, 417

Cordes, J. M. & Lazio, T. J. W. 2002, arXiv reprint:astro-ph, 0207156

Cordes, J. M., Lazio, T. J. W., & McLaughlin, M. 2004, New Astron. Rev., 48, 1459

Cordes, J. M. & Wasserman, I. 2016, Mon. Not. R. Astron. Soc., 457, 232

Costa, A. A. et al. 2022, Astron. Astrophys., 664, A20

Dai, Z. G., Wang, J. S., Wu, X. F., & Huang, Y. F. 2016, The Astrophysical Journal, 829, 27

Dragone, C. 1978, AT T Technical Journal, 57, 2663

Draine, B. T. 2010, Physics of the interstellar and intergalactic medium, Vol. 19 (Princeton University Press)

Eftekhari, T. & Berger, E. 2017, The Astrophysical Journal, 849, 162

Eisenstein, D. J., Zehavi, I., Hogg, D. W., et al. 2005, Astrophys. J., 633, 560

Farah, W., Flynn, C., Bailes, M., et al. 2018, Monthly Notices of the Royal Astronomical Society, 478, 1209

Fedorova, V. A. & Rodin, A. E. 2019, Astronomy Reports, 63, 39–48

Fornazier, K. S. F. et al. 2022, Astron. Astrophys., 664, A18

Gajjar, V., Siemion, A., Price, D., et al. 2018a, The Astrophysical Journal, 863, 2

Gajjar, V. et al. 2018b, Astrophys. J., 863, 2

Gal-Yam, A. 2021, Bulletin of the AAS, 53, https://baas.aas.org/pub/2021n1i423p05

Gardenier, D. W., van Leeuwen, J., Connor, L., & Petroff, E. 2019, Astron. Astrophys., 632, A125

Geng, J. & Huang, Y. 2015, Astrophys. J., 809, 24

Geyer, M., Karastergiou, A., Kondratiev, V. I., et al. 2017, Monthly Notices of the Royal Astronomical Society, 470, 2659

Ghisellini, Gabriele & Locatelli, Nicola. 2018, A&A, 613, A61

Górski, K. M., Hivon, E., Banday, A. J., et al. 2005, Astrophys. J., 622, 759

Gruzinov, A. & Levin, Y. 2019, The Astrophysical Journal, 876, 74

Gu, W.-M., Dong, Y.-Z., Liu, T., Ma, R., & Wang, J. 2016, Astrophys. J. Lett., 823, L28

Hagstotz, S., Reischke, R., & Lilow, R. 2022, Mon. Not. Roy. Astron. Soc., 511, 662

Harris, C. R., Millman, K. J., van der Walt, S. J., et al. 2020, Nature, 585, 357

Heintz, K. E., Prochaska, J. X., Simha, S., et al. 2020, ApJ, 903, 152

Hoyer, S. & Hamman, J. 2017, Journal of Open Research Software, 5

Inoue, S. 2004, Mon. Not. R. Astron. Soc., 348, 999

Ioka, K. 2003, Astrophys. J. Lett., 598, L79

Kashiyama, K., Ioka, K., & Mészáros, P. 2013, The Astrophysical Journal Letters, 776, L39

Kaspi, V. M. & Beloborodov, A. M. 2017, Annual Review of Astronomy and Astrophysics, 55, 261

Katz, J. 2016, The Astrophysical Journal, 826, 226

Katz, J. 2018, Progress in Particle and Nuclear Physics, 103, 1

Katz, J. I. 2018, arXiv reprint:astro-ph, 1804.09092

Keane, E., Johnston, S., Bhandari, S., et al. 2016, Nature, 530, 453

Keane, E. F. 2010, PhD thesis, University of Manchester

Keane, E. F. 2018, Nature Astronomy, 2, 865

Keating, L. C. & Pen, U.-L. 2020, Monthly Notices of the Royal Astronomical Society: Letters, 496, L106

Kellermann, K. I. & Pauliny-Toth, I. I. K. 1969, Astrophys. J. Lett., 155, L71

Kocz, J., Ravi, V., Catha, M., et al. 2019, Monthly Notices of the Royal Astronomical Society, 489, 919

Kraus, J. D., Tiuri, M., Räisänen, A. V., & Carr, T. D. 1986, Radio astronomy, Vol. 69 (Cygnus-Quasar Books Powell, Ohio)

Kulkarni, S., Ofek, E., Neill, J., Zheng, Z., & Juric, M. 2014, The Astrophysical Journal, 797, 70

Kumar, P., Lu, W., & Bhattacharya, M. 2017, Monthly Notices of the Royal Astronomical Society, 468, 2726

Lewis, A. & Bridle, S. 2002, Phys. Rev. D, 66, 103511

Liccardo, V. et al. 2022, Astron. Astrophys., 664, A17

Linder, E. V. 2020, Physical Review D, 101, 103019

Lorimer, D., Karastergiou, A., McLaughlin, M., & Johnston, S. 2013, Mon. Not. Roy. Astron. Soc., 436, 5

Lorimer, D. R., Bailes, M., McLaughlin, M. A., Narkevic, D. J., & Crawford, F. 2007, Science, 318, 777

Lorimer, D. R., Kramer, M., et al. 2005, Handbook of pulsar astronomy, Vol. 4 (Cambridge University Press)

Lu, W. & Kumar, P. 2018, Monthly Notices of the Royal Astronomical Society, 477, 2470

Lu, W., Kumar, P., & Zhang, B. 2020, Monthly Notices of the Royal Astronomical Society, 498, 1397

Luo, R., Lee, K., Lorimer, D. R., & Zhang, B. 2018, Mon. Not. Roy. Astron. Soc., 481, 2320

Luo, R., Men, Y., Lee, K., et al. 2020, Mon. Not. Roy. Astron. Soc., 494, 665

Lyubarsky, Y. 2014, Monthly Notices of the Royal Astronomical Society: Letters, 442, L9

Lyutikov, M., Burzawa, L., & Popov, S. B. 2016, Monthly Notices of the Royal Astronomical Society, 462, 941

Macquart, J.-P., Bailes, M., Bhat, N. D. R., et al. 2010, Publications of the Astronomical Society of Australia, 27, 272

Macquart, J.-P. & Ekers, R. 2018, Monthly Notices of the Royal Astronomical Society, 480, 4211

Macquart, J.-P., Prochaska, J., McQuinn, M., et al. 2020a, Nature, 581, 391

Macquart, J.-P., Prochaska, J. X., McQuinn, M., et al. 2020b, Nature, 581, 391

Macquart, J.-P., Shannon, R., Bannister, K., et al. 2019a, The Astrophysical Journal Letters, 872, L19

Macquart, J. P., Shannon, R. M., Bannister, K. W., et al. 2019b, Astrophys. J. Lett., 872, L19

Madau, P., Meiksin, A., & Rees, M. J. 1997, Astrophys. J., 475, 429

Manchester, R., Taylor, J., & Huguenin, G. 1975, Astrophysical Journal, vol. 196, Feb. 15, 1975, pt. 1, p. 83-102., 196, 83

Marcote, B., Nimmo, K., Hessels, J., et al. 2020, Nature, 1

Margalit, B., Beniamini, P., Sridhar, N., & Metzger, B. D. 2020, The Astrophysical Journal Letters, 899, L27

Margalit, B. & Metzger, B. D. 2018, The Astrophysical Journal Letters, 868, L4

Masui, K., Lin, H.-H., Sievers, J., et al. 2015, Nature, 528, 523

Melrose, D. 2017, Reviews of Modern Plasma Physics, 1, 1

Metzger, B. D., Berger, E., & Margalit, B. 2017, The Astrophysical Journal, 841, 14

Metzger, B. D., Margalit, B., & Sironi, L. 2019, Monthly Notices of the Royal Astronomical Society, 485, 4091

Michilli, D., Seymour, A., Hessels, J., et al. 2018, Nature, 553, 182

Mingarelli, C. M. F., Levin, J., & Lazio, T. J. W. 2015, Astrophys. J., 814, L20

Munoz, J. B., Ravi, V., & Loeb, A. 2020, The Astrophysical Journal, 890, 162

Nicholl, M., Williams, P., Berger, E., et al. 2017, The Astrophysical Journal, 843, 84

Niino, Y. 2018, The Astrophysical Journal, 858, 4

pandas development team, T. 2020, pandas-dev/pandas: Pandas

Papoulis, A. & Unnikrishna Pillai, S. 2002, Probability, Random Variables and Stochastic Processes

Patel, C., Agarwal, D., Bhardwaj, M., et al. 2018, The Astrophysical Journal, 869, 181

Peel, M. W., Wuensche, C. A., Abdalla, E., et al. 2019, Journal of Astronomical Instrumentation, 8, 1940005

Petroff, E., Hessels, J. W. T., & Lorimer, D. R. 2019a, The Astronomy and Astrophysics Review, 27

Petroff, E., Hessels, J. W. T., & Lorimer, D. R. 2019b, Astron. Astrophys. Rev., 27, 4

Petroff, E., Van Straten, W., Johnston, S., et al. 2014, The Astrophysical Journal Letters, 789, L26

Piro, A. L. & Gaensler, B. 2018, The Astrophysical Journal, 861, 150

Platts, E., Prochaska, J. X., & Law, C. J. 2020, The Astrophysical Journal Letters, 895, L49

Platts, E., Weltman, A., Walters, A., et al. 2019, Phys. Rept., 821, 1

Pleunis, Z. 2021

Plotnikov, I. & Sironi, L. 2019, Monthly Notices of the Royal Astronomical Society, 485, 3816

Popov, S. B. & Postnov, K. A. 2013, arXiv preprint arXiv:1307.4924

Price, D. C., Flynn, C., & Deller, A. 2021, Publications of the Astronomical Society of Australia, 38, e038

Price-Whelan, A. M. et al. 2018, Astron. J., 156, 123

Prochaska, J. X. & Zheng, Y. 2019a, Monthly Notices of the Royal Astronomical Society, 485, 648

Prochaska, J. X. & Zheng, Y. 2019b, Monthly Notices of the Royal Astronomical Society, 485, 648

Radhakrishnan, V. & Cooke, D. J. 1969, Astrophysical Letters, 3, 225

Rafiei-Ravandi, M., Smith, K. M., & Masui, K. W. 2020, Physical Review D, 102, 023528

Ravi, V. 2019a, arXiv preprint arXiv:1907.06619

Ravi, V. 2019b, Monthly Notices of the Royal Astronomical Society, 482, 1966

Ravi, V., Catha, M., D'Addario, L., et al. 2019, Nature, 572, 352

Rohlfs, K. & Wilson, T. L. 2013, Tools of Radio Astronomy (Springer Science & Business Media)

Schechter, P. 1976, Astrophys. J., 203, 297

Scholz, P. & Chime/Frb Collaboration. 2020, The Astronomer's Telegram, 13681, 1

Seabold, S. & Perktold, J. 2010, in Proceedings of the 9th Python in Science Conference, ed. Stéfan van der Walt & Jarrod Millman, 92 – 96

Shannon, R., Macquart, J.-P., Bannister, K. W., et al. 2018, Nature, 562, 386

Spitler, L. et al. 2014, Astrophys. J., 790, 101

Spitler, L. G. et al. 2016, Nature, 531, 202

Tendulkar, S. P., Bassa, C., Cordes, J. M., et al. 2017, Astrophys. J. Lett., 834, L7

Thompson, A. R., Moran, J. M., & Swenson, G. W. 2017, Interferometry and synthesis in radio astronomy (Springer Nature)

Thornton, D. e. a., Stappers, B., Bailes, M., et al. 2013, Science, 341, 53

Totani, T. 2013, Publications of the Astronomical Society of Japan, 65, L12

Ulaby, F. T., Moore, R. K., & Fung, A. K. 1981

van Leeuwen, J., Kooistra, E., Oostrum, L., et al. 2023, Astronomy & Astrophysics, 672, A117

Virtanen, P., Gommers, R., Oliphant, T. E., et al. 2020, Nature Methods, 17, 261

Walker, R. 1989, "Sensitivity" in Very Long Baseline Interferometry, ed. M. Felli & RE Spencer (Dordrecht: Kluwer), 163–182

Waxman, E. 2017, The Astrophysical Journal, 842, 34

Wuensche, C. A. et al. 2022, Astron. Astrophys., 664, A15

Yang, Y.-P. & Zhang, B. 2016, Astrophys. J. Lett., 830, L31

Yao, J. M., Manchester, R. N., & Wang, N. 2017, The Astrophysical Journal, 835, 29

Zhang, B. 2016, Astrophys. J. Lett., 827, L31

Zhang, B. 2017, The Astrophysical Journal Letters, 836, L32

Zhang, B. 2018a, Astrophys. J., 854, L21

Zhang, B. 2018b, The Astrophysical Journal Letters, 854, L21

Zhang, B. 2020, Nature, 587, 45

Zhang, B. 2022, arXiv preprint arXiv:2212.03972

Zhang, J. et al. 2022, Astron. Astrophys., 664, A19

Zhou, B., Li, X., Wang, T., Fan, Y.-Z., & Wei, D.-M. 2014, Phys. Rev. D, 89, 107303

Zhu, W., Li, D., Luo, R., et al. 2020, The Astrophysical Journal, 895, L6

Appendix A

Relation between bolometric luminosity and luminosity in Luo et al. (2020)

The energy released per unit of frequency interval in the rest-frame, $E_{\nu'}$, is given by (Lorimer et al. 2013)

$$E_{\nu'} = k\nu'^{\alpha}\,, \tag{A.1}$$

where k is a constant, α is the spectral index and ν' is the rest-frame frequency. The bolometric luminosity is then obtained by integrating the energy over all possible emitted frequencies

$$L_{\rm bol} = \int_0^\infty {\rm d}\nu' E_{\nu'} = \frac{k(\nu'^{\alpha+1}_{\rm high} - \nu'^{\alpha+1}_{\rm low})}{\alpha+1}\,, \tag{A.2}$$

where here we have omitted the top-hat pulse of width present in Lorimer et al. (2013) and $\nu' = (1+z)\nu$.

The luminosity in Luo et al. (2020), however, is a sub-part of the bolometric luminosity, since the assumed spectral width is $\nu_{\rm Luo,\,high} - \nu_{\rm Luo,\,low} = 1$ GHz. We can then write the "Luo" luminosity as

$$L_{\rm Luo} = \int_0^\infty {\rm d}\nu' B_{\nu'} E_{\nu'} = \frac{k\left(\nu^{\alpha+1}_{\rm Luo,\,high} - \nu^{\alpha+1}_{\rm Luo,\,low}\right)}{\alpha+1}(1+z)^{\alpha+1}\,, \tag{A.3}$$

where $B_{\nu'}$ is a rectangular function defined as $B_{\nu'} = 1$ for $\nu'_{\rm Luo,low} \leq \nu' \leq \nu'_{\rm Luo,high}$ and $B_{\nu'} = 0$ otherwise. Note that $L_{\rm Luo} = L_{\rm bol}$ if $\nu'_{\rm high} = \nu'_{\rm Luo,\,high}$ and $\nu'_{\rm low} = \nu'_{\rm Luo,\,low}$.

Using Equations (A.2) and (A.3) we obtain the relation between the two luminosities

$$\frac{L_{\rm bol}}{\nu'^{\alpha+1}_{\rm high} - \nu'^{\alpha+1}_{\rm low}} = \frac{L_{\rm Luo}}{\left(\nu^{\alpha+1}_{\rm Luo,\,high} - \nu^{\alpha+1}_{\rm Luo,\,low}\right)(1+z)^{\alpha+1}} \tag{A.4}$$

Therefore, using the above relation in Eq. (3.10) we obtain Eq. (3.13). The luminosities used in Section 3.3.4 are the "Luo" luminosities $L_{\rm Luo}$, where we have removed the subscript "Luo".